AD/A-003 904

AN EXPERIMENTAL INVESTIGATION OF LATE-STAGE EQUIVALENCE FOR THE AXIAL HYPO-AND HYPERVELOCITY IMPACT OF RODS

J. J. Kelly, et al

North Carolina State University

AD/A-003 904

DOCUMENT CONTROL DATA - R & D

(Security classification of title, body of abstract and indexing annotation must be entered when the overall report is classified)

1. ORIGINATING ACTIVITY (Corporate author)	2a. REPORT SECURITY CLASSIFICATION
NORTH CAROLINA STATE UNIVERSITY Raleigh, North Carolina	Unclassified
	2b. GROUP

3. REPORT TITLE

AN EXPERIMENTAL INVESTIGATION OF LATE-STAGE EQUIVALENCE FOR THE AXIAL HYPO- AND HYPERVELOCITY IMPACT OF RODS

4. DESCRIPTIVE NOTES (Type of report and inclusive dates)

Technical Report

5. AUTHOR(S) (First name, middle initial, last name)

J. J. Kelly and R. A. Douglas

6. REPORT DATE	7a. TOTAL NO. OF PAGES	7b. NO. OF REFS
November, 1974	93	31

8a. CONTRACT OR GRANT NO.	9a. ORIGINATOR'S REPORT NUMBER(S)
N00014-68-A-0187	
b. PROJECT NO.	74-3
c.	9b. OTHER REPORT NO(S) (Any other numbers that may be assigned this report)
d.	

10. DISTRIBUTION STATEMENT

Approved for public release; Distribution unlimited

11. SUPPLEMENTARY NOTES	12. SPONSORING MILITARY ACTIVITY
	Office of Naval Research

13. ABSTRACT

This report describes the development of a diffraction-grating strain-measurement system capable of measuring axial surface strains in target rods experiencing axial hypo- and hypervelocity impact and its subsequent application to evaluate the existence of the late-stage equivalence principle for this impact configuration.

From an analysis of the material-point strain histories collected from long (> 21 diameters), polycarbonate target rods axially impacted by equal diameter (0.743 in), short (< 2 diameters), polycarbonate projectiles traveling at velocities from 10,980 ft/sec to 15,476 ft/sec, it was concluded that:

1) Late-stage equivalence does exist for target configurations other than the previously investigated semi-infinite solid case, and

2) the value of the exponent α in the scaling law $L_o V_o^\alpha = L_1 V_1^\alpha$ was determined to be 1.32 for the target configuration of this investigation.

DD FORM 1473 (PAGE 1)
S/N 0101-807-6811

14. KEY WORDS	LINK A		LINK B		LINK C	
	ROLE	WT	ROLE	WT	ROLE	WT
Hypervelocity Impact						
Late-Stage Equivalence						
Polycarbonate						
Diffraction Grating Strain Transducer						

DD FORM 1473 (BACK)
S/N 0101-807-6921

i&

NORTH CAROLINA STATE UNIVERSITY
Raleigh, North Carolina

AN EXPERIMENTAL INVESTIGATION OF LATE-STAGE EQUIVALENCE

FOR THE AXIAL HYPO- AND HYPERVELOCITY IMPACT OF RODS

J. J. Kelly and R. A. Douglas

Technical Report 74-3   November, 1974

ABSTRACT

This report describes the development of a diffraction-grating strain-measurement system capable of measuring axial surface strains in target rods experiencing axial hypo- and hypervelocity impact and its subsequent application to evaluate the existence of the late-stage equivalence principle for this impact configuration.

From an analysis of the material-point strain histories collected from long (> 21 diameters), polycarbonate target rods axially impacted by equal diameter (0.743 in), short (< 2 diameters), polycarbonate projectiles traveling at velocities from 10,980 ft/sec to 15,476 ft/sec, it was concluded that:

1) Late-stage equivalence does exist for target configurations other than the previously investigated semi-infinite solid case,

and 2) the value of the exponent α in the scaling law $L_o V_o^\alpha = L_1 V_1^\alpha$ was determined to be 1.32 for the target configuration of this investigation.

TABLE OF CONTENTS

LIST OF TABLES

LIST OF FIGURES

LIST OF FIGURES   (continued)

1 Introduction

1.1 Preliminary Problem Definition

The term hypervelocity impact is used to denote a projectile-target collision where the magnitude of the relative striking velocity is at least twice the magnitude of the elastic wave speed of the target. Impact velocities slightly less than this value but still in this regime are referred to as hypovelocity impacts. Except for the particle velocities achieved through the detonation of shaped charges, these impact velocities are typically an order of magnitude greater than those created by traditional ballistics and the natural occurrence of impacts at these extreme velocities is realized primarily in the environment of outer space. Due to the presence of meteoroids and space particles traveling at speeds of from 36,000 to 230,000 feet per second, the possibility exists that any solid surface in space will be subjected to such an impact (1); therefore, the necessity of providing protection for spacecraft instrumentation and personnel has stimulated a strong interest in the phenomena characteristic of hypervelocity impact. These phenomena include shock, plastic, and elastic wave propagation resulting in melting and resolidification, vaporization and condensation, and microstructural phase changes of the materials involved.

Due to the unusually severe conditions occurring during hypervelocity impact, experimental and theoretical investigations have proven extremely difficult. Experimental investigations have had to develop means of accelerating projectiles to the required extreme velocities and to develop techniques suitable for measurement of the large transient deformations. Theoretical analyses attempting to quantitatively model the deformations

have been confronted with the solution of field equations which are highly non-linear and must include equations of state to describe the material while in the vapor, condensed plastic and elastic states. The intensive investigative efforts of the 60's have provided a wealth of information about shock propagation and wave interaction in solids experiencing hyper-velocity impact and the capability, through either empirically developed equations or analytically modeled computer codes, to predict the terminally observed deformations.

Additionally, these investigations have provided some general principles relating to the behavior of material configurations subjected to hypervelocity impact; however, due to the wave propagation generated by such an impact, the validity of these principles is particularly sensitive to the choices of projectile-target geometries and materials. One principle which seems to defy these limitations is the late-stage equivalence principle, proposed by J. M. Walsh (2) for the configuration of normal hypervelocity impact of a projectile against the flat surface of a semi-infinite solid. Based on analysis of his computer code modeling of the initial transient target response as a compressible inviscid fluid, Walsh stated that:

> "One result of the early impact calculations was to show that two like-material impacts at different velocities lead to the same late-stage flow when the projectiles are characterized by the same value of $L_o V_o \alpha$, where L_o denotes a characteristic dimension of the projectile, V_o the impact velocity, and α was determined to be about 0.58. It was also shown that at high velocities that late-stage flow does not depend on the density of the projectile and

the details of its shape except through their influence on the
mass M (provided neither the density ratio nor the shape is too
extreme)."

Significantly, no restrictions are placed on variations of projectile
shape (only on the target) and the only restriction on material selection
is that projectile and target should be the same. Walsh feels that
additional significance (section 1-3) is implied by the value of the
exponent α, since this scaling law ($L_o V_o \alpha = L_1 V_1 \alpha$) represents neither
conservation of momentum nor conservation of energy (where the value of
α would be 1/3 and 2/3 respectively).

Although this correlation was discovered from computations omitting
the presence of material dissipation mechanisms, Walsh surmised that it
became useful if one observes that this equalization of flows occurs as
a result of the interaction of shock waves having magnitudes which are
much greater than the material strengths. Hence, the strength affected
phase would be subsequent to this initial equalization and therefore
should be the same also.

The work described here encompassed the development of a diffraction
grating strain measurement technique capable of accurately measuring the
large strains and strain rates resulting from a hypo or hypervelocity
impact and its subsequent application to test the validity of the late-
stage equivalence principle for a new target shape having finite lateral
dimensions.

More precisely, the impact problem under consideration was that of
the axial impact (at hypo and hypervelocity speeds) of a free flight
projectile with a target rod which is initially at rest. Both projectile

and target were rods of circular cross section, with the same diameter and of the same material (polycarbonate). Material selection was based on its compatibility with the diffraction grating technique (previously measured dynamic strains of 20% and strain rates of 16,000 sec^{-1} (21)) as well as its relatively low elastic wave speed ($\simeq$ 7500 feet per second).

The premise of this investigation has been that for the same material, equivalent impacts would at some time produce exactly the same deformation, and that the resulting wave propagation would be indicative of this equivalence (i.e., material points having identical positions in targets experiencing equivalent impacts would exhibit identical deformation histories). Acting under this premise, families of strain histories were collected from target rods experiencing different impact conditions (characterized by projectiles having different values of L_o and V_o) and used to test for late-stage equivalence. Late-stage equivalence was assumed to exist if the families of strain histories from two different impacts were the same.

1.2 The Phenomenology of Hypervelocity Impact

Research in hypervelocity impact has been directed in the main toward the solution of a specific problem· the quantitative prediction of the deformation resulting from the impact of space particles, traveling at meteoric speeds, with spacecraft surfaces. This real situation has been generally investigated by examining the deformation produced by the normal hypervelocity impact of projectiles against flat solid surfaces. Experimental work has examined the effects of changing projectile velocity, shape, mass, and material upon the penetration of plates or the crater depth produced in thicker plate configurations (3). Measurements have ranged from terminal observation of hole size or crater depth in engineering materials, to the transient measurements of shock penetration and strength in wax by J. T. Frasier (1,11).

Theory development and solution has ranged from the extensive work of J. M. Walsh (4) and W. J. Rae (5) with their computer analyses of the transient behavior of a semi-infinite solid impacted by a projectile traveling at hypervelocity speeds, to the approximate, steady-state, one-dimensional solutions for crater depth of S. W. Yuan (6,7).

The results of those investigations provide the following description of the transient material response and wave propagation resulting from hypervelocity impact. The hypervelocity impact of a solid projectile against a solid target produces shock waves in the projectile and target which are initially of megabar proportions and orders of magnitude greater than even the ultimate strengths of the materials involved. Since the maximum resolved shear stress resulting from these shocks is so much larger than that which the materials can withstand, initial

material response is characterized as that of a compressible inviscid
fluid. Experiments have shown (1,11), however, that these initial impact
pressures are quickly attenuated to values in the vicinity of ordinary
material strengths through the action of relief waves which result from
material expansion at projectile and target free boundaries. Subsequent
material response is assumed to be that of a plastically deforming solid
which further attenuates the wave and finally arrests the deformation.

As a physical model, consider the normal (incidence) hypervelocity
impact of a cylindrical projectile against the flat surface of a like
material semi-infinite solid. As indicated in Figure 1.2.1 the impact
simultaneously initiates a shock wave (S_1) which travels forward into
the target as well as a rear facing shock (S_2) which travels back into
the target. Due to the radial expansion of the projectile and target a
rarefaction wave (R_1) is transmitted toward the axis of symmetry and
serves as a source of lateral attenuation for both the shocks S_1 and S_2.
Upon arrival of the shock front S_2 at the rear of the projectile, the
boundary condition of zero pressure at this surface results in the
reflection of this shock as another rarefaction (R_2). As depicted in
Figure 1.2.2, the wave pattern now consists of the target shock S_1 moving
forward into the target and the rarefactions R_1 and R_2 which rapidly over-
take and attenuate the target shock.

It is these relaxation waves which comprise the equilibrating mecha-
nism to produce late-stage equivalence (i.e., the principle essentially
provides initial conditions under which two different impacts will produce
the same late-stage pressure distribution in the targets after the
arrival of attenuation waves from the sides and rear of the projectile).

Figure 1.2.1 Estimated Wave Pattern After Impact

Figure 1.2.2 Estimated Wave Pattern After Reflection
of Projectile Shock S_2

Depending on the projectile aspect (length to width) ratio, the wave pattern depicted in Figure 1.2.2 (and the resulting target shock attenuation) can have many variations. For example, the schematic of Figure 2 assumes that the projectile is short enough that the central portion of the projectile shock S_2 can reach the rear surface of the projectile and be reflected without having been previously attenuated by the lateral rarefaction wave R_1. Since the magnitude of the rarefaction R_2 is dependent upon the magnitude of the shock S_2 immediately prior to its reflection (15) this primary wave interaction can strongly affect the terminal wave interaction which attenuates the target shock S_1.

Due to the simultaneous presence of many types of waves and the complexities introduced by their resulting interactions, characterizational statements about the attenuation of shocks by the geometricallv dependent rarefactions are tied to particular projectile configurations.

One such characterization is found in the fundamental investigations of shock attenuation carried out by Al'tshuler, et.al. (16). In part of these investigations, the attenuation of forward facing shocks by lateral rarefaction waves was utilized to determine the compressed material sound speeds for aluminum, copper, lead, and iron. The test configuration was the inverse of the previously stated problem (i.e., a thick slab projectile having large lateral dimensions normal impacting an initially stationary short cylindrical target). For this configuration, with the axial and transverse dimensions of the projectile much larger than those of the target, initial shock attenuation in the cylindrical target results from the rarefaction waves originating at the target circumference of the impact face. Since measurements were taken prior to the arrival of other types of rarefactions, general characterizational

information was obtained in addition to the aforementioned sound speeds.
As an integral part of the measurement technique it was found that the
distance the shock wave had traveled into the target by the time the
rarefaction waves had arrived at the target axis of symmetry (and hence
had provided attenuation to all of the target shock front) could be
characterized by:

$$h = \frac{d}{2} \ \frac{1}{Tan \ \gamma} \qquad\qquad (1.2.1)$$

where

        h = the axial distance from the original impact plane,

        d = the diameter of the cylindrical target,

        γ = a parameter dependent upon material properties.

Significantly, it was found that for strong shocks the value of
Tan γ was bounded in the narrow interval of 0.66 to 0.73 for a wide range
of materials (metals, plastics, water). The authors concluded that (16):

    "Apparently it is possible to use the value Tan γ = 0.7

    for very strong shock waves in other materials also."

In a more recent investigation, DiBattista (17) impacted short
cylindrical polycarbonate projectiles against the flat surface of poly-
carbonate plates (confirming to the configuration of Figure 1.2.1 and
utilizing the materials of this study) and concluded that "h" was about
one-half the value indicated by using Tan γ = 0.7 in Al'tshuler's
expression. No attempt is made to explain this measured discrepancy and
since polycarbonate was not a material investigated by Al'tshuler et. al.,
one is left to wonder whether the shocks of DiBattista's experiments were
not strong enough or whether polycarbonate is a material not to be included

in the characterization; however, the value measured by DiBattista appears
to be invariant since the distance required for lateral attenuation was
the same for the two velocity levels investigated.

Noting the previously discussed dependences on projectile-target
geometries and materials, let us qualitatively represent the sequence of
events in the model by a plot of the target shock magnitude versus target
shock position shown in Figure 1.2.3. For some distance (X_a) the target
shock travels unattenuated into the target and possesses a magnitude many
times the ordinary material strength. At this distance, depending on the
projectile aspect ratio, either the rarefaction R_1 or R_2 overtakes the
wave and begins to drop the shock to a lower pressure (P_b) at which point,
(X_b), the remaining rarefaction further attenuates the shock.

More quantitatively let us assume the projectile-target material to
be polycarbonate and the projectile to be 0.406 cm. in length and have a
radius of .284 cm. (aspect ratio = L/D = 0.71). Then the measurements of
DiBattista show (17):

"For projectile impacts at 6.4 and 7.4 Km/sec the shock-wave

pressure at the impact axis remained constant at 0.282×10^{11}

and 0.355×10^{11} Newtons/M^2, respectively, to a shock wave

penetration near 75 percent of the projectile radius. It should

be noted that the shock wave penetration 0.75rp to which the

shock-wave pressure remained constant was approximately one-half

the expected value. Near this shock wave penetration, the

rarefaction wave, originating from the free boundary of the

interface between the target and projectile, arrived at the

impact axis and the shock-wave pressure rapidly decreased to

Figure 1.2.3 Peak Target Shock Pressure Versus
Shock Position along the Axis of Symmetry

pressures near 0.085×10^{11} Newtons/M^2 at shock wave penetrations near 3.10 and 3.30 projectile radii, respectively. At these penetration depths, the shock-wave pressure again decreased because of a rarefaction wave which originated at the projectile near surface and the shock-wave pressures became inversely proportional to the shock-wave penetration raised to approximately the 2.5 power for shock-wave penetrations as great as 7.0 projectile radii."

1.3 Late Stage Equivalence

Since experiments on hypervelocity impact are limited in velocity to about 35,000 feet per second, for "apriori" knowledge of projectile configuration, theorists searched for a scaling law which would provide a comparison of laboratory measurements with the computer calculations at much faster velocities. Motivated by the conservation laws, investigators have attempted to establish both momentum (8) and energy (9,10) as being the single dominant parameter affecting hypervelocity impacts; however, based on his computer calculations of the deformations and pressure distributions created by hypervelocity impacts during the first phase of target response (modeled as compressible inviscid fluid flow), J. M. Walsh proposed (2,4) that the dominant parameter was neither momentum nor energy but a parameter intermediate to these quantities.

From a systematic comparison of calculated results for a number of impacts, it was found that (4):

"the late-stage flow was unchanged when the projectile size L_o and the velocity V_o were varied in such a way that $L_o V_o \alpha$ remained constant. More precisely it was found that at late times the velocity, pressure and density profiles in both the axial and radial directions were asymptotically the same for pairs of projectiles characterized by the same value of $L_o V_o \alpha$. The value of α determined was 0.58 ± 0.01 for a wide range of velocities and materials."

The particular characterization of such projectile parameters as geometry, mass, and velocity by the single parameter $L_o V_o \alpha$ arises from a dimensional analysis of the analytically intractable impact problem

and is the end result of hypothesizing that all such variables can be included in one general product term. In order to clarify that parameter's previous comparison with the quantities of projectile momentum and energy, let us consider the following brief formulation.

Guided by the physical realities and mathematical formulations of the conservation laws of momentum and energy, assume that the effects of porjectile mass, velocity and geometry can be characterized by the quantity MV^β where M is the projectile mass, V is the projectile velocity and β is some unknown exponent. Further assume that if this quantity is kept constant for two different impacts, then the resulting target deformations from those impacts would be the same; hence, a scaling law permitting the prediction of required projectile mass (M_1) and velocity (V_1) to produce the same deformation as a known reference impact characterized by projectile mass (M_0) and velocity (V_0) could be written as:

$$M_0 \, V_0^\beta = M_1 \, V_1^{\ \beta} \, . \tag{1.3.1}$$

Let us rewrite the projectile masses as:

$$M_0 = \text{density (volume)} = \gamma_0 \, (\theta_0 L_0^{\ 3}), \tag{1.3.2}$$

and $$M_1 = \text{density (volume)} = \gamma_1 \, (\theta_1 L_1^{\ 3}), \tag{1.3.3}$$

where L_0 and L_1 are assumed to be characteristic dimensions of the two projectiles. Substitution of expressions (1.3.2) and (1.3.3) into (1.3.1) yields:

$$\gamma_0 \, (\theta_0 L_0^{\ 3}) \, V_0^{\ \beta} = \gamma_1 \, (\theta_1 L_1^{\ 3}) \, V_1^{\ \beta} \, . \tag{1.3.4}$$

For projectiles having the same material density and volumetric constants, $\gamma_0 = \gamma_1$, $\theta_0 = \theta_1$ and,

$$L_o^3 \, V_o^\beta = L_1^3 \, V_1^\beta \qquad (1.3.5)$$

$$\text{or} \quad L_o \, V_o^\alpha = L_1 \, V_1^\alpha \quad (\text{where } \alpha = \beta/3) \qquad (1.3.6)$$

Observing the formulations for momentum (MV) and energy ($1/2 \, MV^2$) and noting the exponent relationships from equation (1.3.6), one can write similarly stated relationships for these quantities:

$$L_o \, V_o^{1/3} = L_1 \, V_1^{1/3} \quad (\text{Momentum}) \qquad (1.3.7)$$

$$L_o \, V_o^{2/3} = L_1 \, V_1^{2/3} \quad (\text{Energy}) \qquad (1.3.8)$$

Comparison of equations (1.3.6), (1.3.7), and (1.3.8) shows that Walsh's late-stage equivalence principle amounts to preserving neither momentum nor energy, but a new quantity, intermediate to them, which is dependent on both.

It is noted that as originally proposed, Walsh's principle was based on calculations made for the first-stage of hypervelocity impact with projectile and target material characterized as compressible inviscid fluids and without having taken into account possible material strength effects; however, Walsh surmised that if indeed equalization of shock pressures occurred during the extreme pressure regime, where these assumptions seemed valid, then subsequent target response in the strength effected regime would be the same for targets having the same strength properties.

Experimental verification of the hydrodynamic computer code is offered in a presentation by Frazier (11) of his measurements of shock speeds and stresses resulting from the hypervelocity impact of ethocel cylinders against wax targets. Shock velocities and stresses as functions

of position in the target are presented for two nominal velocities
(13.200 feet per second and 19,600 feet per second) with comparisons
of matching calculations from the hydrodynamic code. Agreement is quite
good for both velocity levels for distances up to 1 inch where shock
pressure had dropped to within an order of magnitude of the strength
of the target material.

Subsequent refinements of the computer code were made to include
strength effects and the updated code was used to calculate terminal
deformations for comparison with experimentally determined values.
Surprisingly, however, the two experiments chosen for comparison are
identical except for target strength with no variations in impact con-
ditions. Projectile velocity, geometric dimensions, and mass were the
same for impacts into hard and soft aluminum. Predicted final crater
geometries (depths) are within 2% for the soft aluminum and 12% for
the hard aluminum. As a measure of the code's ability to predict the
transient target response, Walsh offers a comparison of shock particle
velocity as a function of distance into the target with experimentally
determined values for the impact of a soft aluminum sphere against a
like material target. The agreement between experiment and calculation
is within 20% for velocities above 10^4 cm/sec (equivalent to ~15 kbars
pressure) but falls to 50% for comparisons below this value. With
these comparisons providing justification of the validity of the com-
puter calculations, Walsh uses the code to examine the late-stage equi-
valence principle. The results of these calculations can be summarized as
follows:

1) the impact velocity should be greater than about twice
the target sound speed,

2) the principle is applicable to a wide range of like
   material impacts (projectile and target of the same
   material) with comparisons shown for iron, aluminum,
   lead, and polyethelene.

3) comparison of various projectile geometries (sphere,
   cylinder, rod, disc) showed that the projectile length to
   width ratio should not be greater than three,

4) late is the time required for the projectile to travel
   about three times its length,

5) the value of $\alpha = 0.58$ is for the axisymmetric problem
   of normal impact of a projectile against the flat
   surface of a semi-infinite solid.

In an investigation of the characterization of projectile parameters
by the single quantity $L_o V_o^\alpha$, Dienes (4,12) examines the extreme case,
and more analytically tractable case, of the projectile having a finite
short length and infinite width. The author concludes from a similarity
solution for this planar wave case that (4):

"...the flow is characterized by a quantity $L_o V_o^\alpha$
intermediate between energy and momentum. The value of
α depends on the equation of state of the target material
and varies between 1.0 and 1.79 in the case of an ideal-
gas target."

How can the values of α for this case be bounded by the exponents
for momentum and energy, when according to equations (1.3.7) and (1.3.8)
these exponents are 1/3 and 2/3 respectively? This seeming anomaly can
be clarified by a return to the assumptions of the previous derivation
(1.3.1) → (1.3.6). In equations (1.3.2) and (1.3.3), it was assumed
that projectile volumes could be represented as θL^3 where L is a charac-

teristic dimension, whose change would automatically result in scaled changes of the other two dimensions. Instead, let us now represent projectile volume as XYL where X and Y represent projectile lateral dimensions unaffected by a change in L. Equating the momentum and energy for two different impacts would now have the form:

$$\gamma_o \ (\theta_o X_o Y_o L_o) \ V_o = \gamma_1 \ (\theta_1 X_1 Y_1 L_1) \ V_1 \quad \text{(momentum)} \quad (1.3.9)$$

$$\gamma_o \ (\theta_o X_o Y_o L_o) \ V_o^2 = \gamma_1 (\theta_1 X_1 Y_1 L_1) \ V_1^2 \quad \text{(energy)} \quad (1.3.10)$$

Now, for comparison of impacts in which the projectiles have equal density and the same product of lateral dimensions we have:

$$L_o \ V_o = L_1 \ V_1 \quad \text{(momentum)} \quad (1.3.11)$$

$$\text{and} \quad L_o \ V_o^2 = L_1 \ V_1^2 \quad \text{(energy)} \quad (1.3.12)$$

Hence, for the one-dimensional impact of the planar wave case the bounds of momentum and energy are represented by the exponents 1 and 2 respectively.

Additional justification of the late-stage equivalence principle for this planar wave case is found in the numerical solutions of Chou and Burns (13) and the experiments of Chou and Allison (14). Chou and Burns used the method of characteristics to examine the impact problem for five different materials (aluminum, copper, and ideal gas) with values of specific heat ratios given by 1.1, 1.4, and 2.0 and determined the exponent α for each material. For each material, a standard impact case was calculated first. Other cases with the same material properties but having different projectile thicknesses and impact velocities were then calculated for a comparison with standard case. The criteria used

for establishing late-stage equivalence were that plots of shock position in the target versus time as well as peak pressure distributions be the same. For impacts satisfying these criteria, the value of α was determined by inserting the appropriate impact conditions in equation (1.3.6). The results of this investigation are in agreement with those of Dienes, yielding values of α for the ideal gas cases from 1.3 to 1.62 and values of 1.28 and 1.50 for aluminum and copper respectively.

Explicit experimental verification of the value for aluminum is found in the earlier work of Chou and Allison. Using 1100F aluminum as the test material, the authors experimentally determined wave arrival times and peak pressure distributions for a standard case and two comparison cases. The criteria for the existence of late-stage equivalence were the same as for the characteristic solutions of Chou and Burns resulting in a value of $\alpha = 1.33$. Also included in this publication are characteristic solutions which predict α to be 1.27. This discrepancy between analytically predicted and experimentally determined results is deemed insignificant by the authors since the calculations yielded results which were not too sensitive to the value of α and satisfactory comparisons could be made for values of α from 1.25 to 1.30.

For comparison, the results of the previous discussions are summarized in Table 1 and the following observations are noted from this comparison:

1) within the projectile length to width ratios and
   restrictions placed by Walsh, the axisymmetric case
   is the same for a wide range of materials,

2) the extreme projectile configuration producing the
   plane wave case is sensitive to a change in projectile-
   target material yet is bounded by the exponents for
   momuntum and energy for this configuration,

3) in all investigations, the target configuration was that of a flat surface with infinite length and lateral dimensions.

TABLE 1.3.1 EVALUATIONS OF THE EXPONENT α IN THE

LATE –STAGE EQUIVALENCE PRINCIPLE $L_o V_o^\alpha = L_1 V_1^\alpha$

α	PROJECTILE CONFIGURATION	TARGET CONFIGURATION	RESULTING WAVE PROPAGATION	PROJECTILE TARGET MATERIAL	MEANS OF EVALUATION	INVESTIGATORS
0.58	SPHERE, ROD, CULINDER, DISC (WHERE $\frac{1}{3} < \frac{\text{LENGTH}}{\text{WIDTH}} < 3$)	SEMI–INFINITE SOLID	THREE DIMENSIONAL AXISYMMETRIC	IRON, ALUMINUM LEAD, POLY–ETHELENE	ANALYTICAL (HYDRODYNAMIC COMPUTER CODE)	WALSH
1–1.79	THIN SLAB OF INFINITE TRANSVERSE DIMENSIONS	"	ONE DIMENSIONAL PLANE WAVE	IDEAL GAS $\gamma = 1.0$	ANALYTICAL (SIMILARITY ANALYSIS)	DIENES
1.5	"	"	"	$\gamma = 1.4$		
1.3	"	"	"	IDEAL GAS	ANALYTICAL (CHARACTERISTIC SOLUTIONS)	CHOU AND BURNS
1.5	"	"	"	$\gamma = 1.1$ $\gamma = 1.4$		
1.62	"	"	"	$\gamma = 2.0$		
1.28	"	"	"	ALUMINUM	"	
1.5	"	"	"	COPPER	"	
1.33	THIN SLAB	"	"	ALUMINUM 1100F	EXPERIMENTAL	CHOU AND ALLISON

1.4 Hypervelocity Impact of Rods

As indicated in the previous sections, the configuration of prime
interest to those involved in hypervelocity impact research has been that
of the impact of a projectile against a plate. Practically all of the
measurements and development of theory have been directed toward investi-
gation of this configuration. Attempts to simplify the analysis and
measurements to those of a one-dimensional state generally ended in
study of the one-dimensional strain state produced by the planar impact
of plates. The general availability of the shock wave analysis and
transient measurement techniques for the resulting large deformations
employed by those investigations provided a natural bias toward this
approximation.

It is not surprising, therefore, that a search of the literature
yielded only one publication concerned with the hypervelocity impact of
rods. That investigation (18) was a postmortem study of the hypervelocity
impact of rods where the bar axes were perpendicular to each other and
to the velocity vector. Since the configuration was not that of axial
impact and the measurements were not of transient deformations, the
investigation bears little resemblance to the present work.

The greatest number of publications concerning the axial impact of
rods is found in the field of dynamic constitutive equation evaluation,
where this configuration is used to produce a dynamic one-dimensional
stress state; however, these investigations have generally studied
deformations resulting from impact velocities of much less than 2000 feet
per second. The investigations of J. F. Bell (19,20) are representative
of the extensive work which has been done to examine the plastic wave

propagation created by the axial impact of rods within this range of loadings. Using diffraction grating strain gages to provide accurate finite strain-time profiles, Bell has examined the one-dimensional stress response of a wide variety of crystalline solids. Based upon the results of many experimental investigations (19), Bell has proposed a rate-independent dynamic constitutive equation and recent investigations (20) have been concerned with temperature dependence rather than extensions to higher rates of loading.

Another group which has enjoyed considerable success with the diffraction grating strain sensor is the THEMIS research group headed by R. A. Douglas (21,22,23). Thi group has used a diffraction grating technique to extend the ability for accurate measurement of large strains and high strain rates created by impact velocities much faster than those of J. F. Bell (1800 feet per second vs 500 feet per second). Measurements have been taken in structural materials such as steel and aluminum as well as in impact resistant materials such as polycarbonate.

An investigation of the wave propagation resulting from an impact velocity exceeding the normal range of investigation was carried out by Valather and Baker (24). The authors considered the axial impact of an aluminum projectile rod with a like-material target rod which was initially at rest. The impact velocity was 8000 feet per second and corresponds to about one-half the elastic wave speed of aluminum. At various axial positions along the target rod, electrical resistance strain gages were used to record the transient axial deformations; however, due to failure of the gages near the impact face, only deformations at axial distances greater than four diameters away from the impact face were measured. Since these gages were not capable of responding to

the deformations created at an impact velocity which is about one-fourth the velocity needed to achieve hypervelocity impact, it was felt that any successful extension of measurements into the hypervelocity region would be through the application of diffraction grating strain gages.

In conclusion, it is noted that no quantitative measurements of transient deformation have been accomplished for the one-dimensional stress configuration produced by the axial hypervelocity impact of rods.

2 The Reflective Diffraction Grating as a Strain Transducer

2.1 Introduction

A reflective diffraction grating is composed of a set of equidistant parallel grooves (lines) which are impressed into a solid surface. If the grating is illuminated by a monochromatic collimated light source, then issuing from the grating will be the reflected ray and a set of diffraction rays. The angular separation of the rays is dependent upon the angle of incidence of the attacking ray, the line spacing of the grating, and the wave length of the incident light. Any change in line spacing, due to deformation of the grating, is indicated by a change in angular separation of the diffracted rays. Under well chosen conditions, it is possible to determine transient deformation of the grating by recording the motion of either i) any two of the diffracted rays or 2) one diffracted ray and the reflected ray. The following derivation of the diffraction strain relationships will serve to elaborate upon these restrictions and provide the basic requirements for a diffraction-grating strain measurement system.

2.2 The Diffraction-Strain Relationships

Consider that a diffraction grating is impressed into the surface of a test piece and that the perpendicular distance between the grooves (lines) is d_o. If the test piece is then deformed such that the perpendicular distance between the lines is now d, then the Lagrangian extension perpendicular to the lines of the grating is

$$E_L = \frac{d-d_o}{d_o} \quad . \tag{2.2.1}$$

Since,

$$d_o = \frac{1}{m_o}$$

$$\text{and} \quad d = \frac{1}{m} \tag{2.2.2}$$

where

m_o = initial line density

m = line density after deformation

Equation 2.2.1 becomes

$$E_L = \frac{m_o - m}{m} \tag{2.2.3}$$

As was previously mentioned, when the grating is illuminated with a monochromatic collimated light, then the angular position of the diffracted orders is dependent upon the line density of the grating. Therefore, to make equation (2.2.3) a usable expression, one need only obtain expressions for m_o and m in terms of measurable quantities. With this motivation, consider Figure (2.2.1) and the following assumptions: if

1) the direction of the incident collimated light lies in the plane normal to the grating (the x-y plane of Figure 2.2.1),

2) during deformation the grooves of the grating remain parallel to the z axis,

and

3) the only component of surface rotation during deformation is about the z axis,

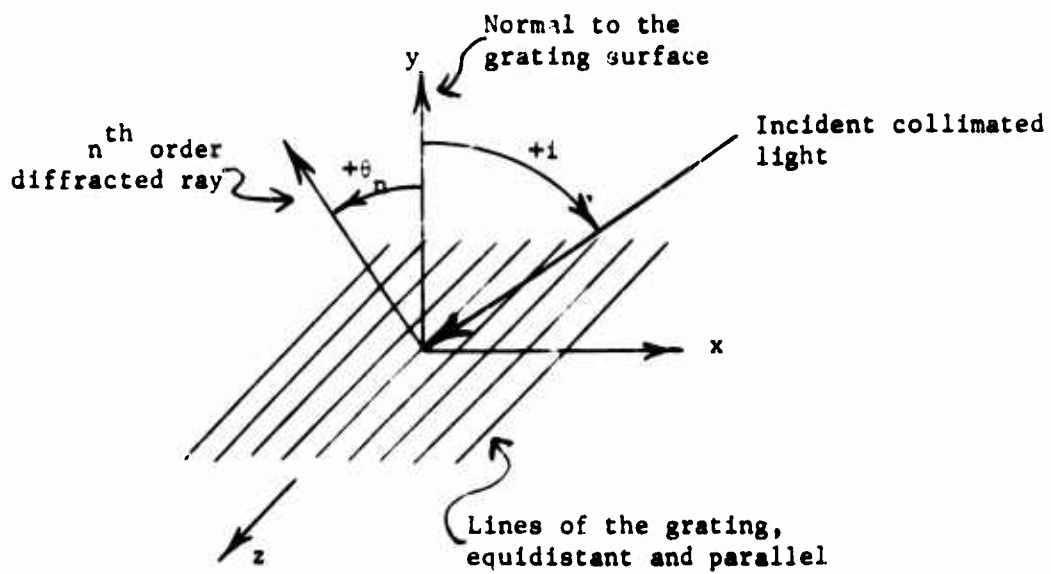then the reflected ray and the diffracted rays lie in the x-y plane and (25)

Figure 2.2.1 Sign Convention for the Incident and
Diffracted Ray Angles of the Diffraction
Equation

$$\sin \theta_n - \sin i = nm\lambda \qquad\qquad (2.2.4)$$

where

      n = the order of interference of a particular diffracted

         ray; it may be zero or a positive or negative integer,

      θ_n = the angle between the normal to the grating surface

         and the nth order diffracted ray, positive as shown

         in Figure 2.1,

      i = the angle between the normal to the grating surface

         and the incident collimated light, positive as shown

         in Figure 2.1,

      m = the number of grooves (lines) per unit length of the

         diffraction grating,

and

      λ = the wave length of the incident collimated light.

Although equation (2.2.4) provides a functional relationship for m in terms of the diffraction angles θ_n, it is practically useless for dynamic experimental application since the angles are referred to the instantaneous grating normal position. A much more useful expression can be obtained by restating equation (2.2.4) in terms of initial (un-strained) diffraction angles and angular shifts of the diffracted rays due to surface rotation and normal strain. Hence consider Figure 2.2.2 where

      θ_{ko}, θ_k = the initial and final k^{th} order diffraction

         angles,

      θ_{no}, θ_n = the initial and final n^{th} order diffraction

         angles,

i_o, i = the initial and final angles of incidence,

ω = the rotation of the diffraction grating surface, positive counterclockwise,

$\Delta\psi_k$ = the a le change of the kth diffracted order, positive counterclockwise,

and

$\Delta\psi_n$ = the angle change of the nth diffracted order, positive counterclockwise.

For normal strain (deformation perpendicular to the lines of the grating) and grating surface rotation only about a line parallel to the lines of the grating, consideration of the nth diffracted order and equation (2.2.4) gives

$$n\lambda m = \sin(\theta_{no} + \Delta\theta_n) - \sin(i_o + \Delta i) \qquad (2.2.5)$$

From Figure 2.2.2,

$$\Delta i = i - i_o = \omega \qquad (2.2.6)$$

$$\Delta\psi_n + \theta_{no} = \theta_n + \omega \qquad (2.2.7)$$

$$\Delta\psi_k + \theta_{ko} = \theta_k + \omega \qquad (2.2.8)$$

From equations (2.2.7) and (2.2.8),

$$\Delta\theta_n = \theta_n - \theta_{no} = \Delta\psi_n - \omega \qquad (2.2.9)$$

$$\Delta\theta_k = \theta_k - \theta_{ko} = \Delta\psi_k - \omega \qquad (2.2.10)$$

Substituting equations (2.2.9) and (2.2.10) into (2.2.5) gives

$$n\lambda m = \sin(\theta_{no} + \Delta\psi_n - \omega) - \sin(i_o + \omega) \qquad (2.2.11)$$
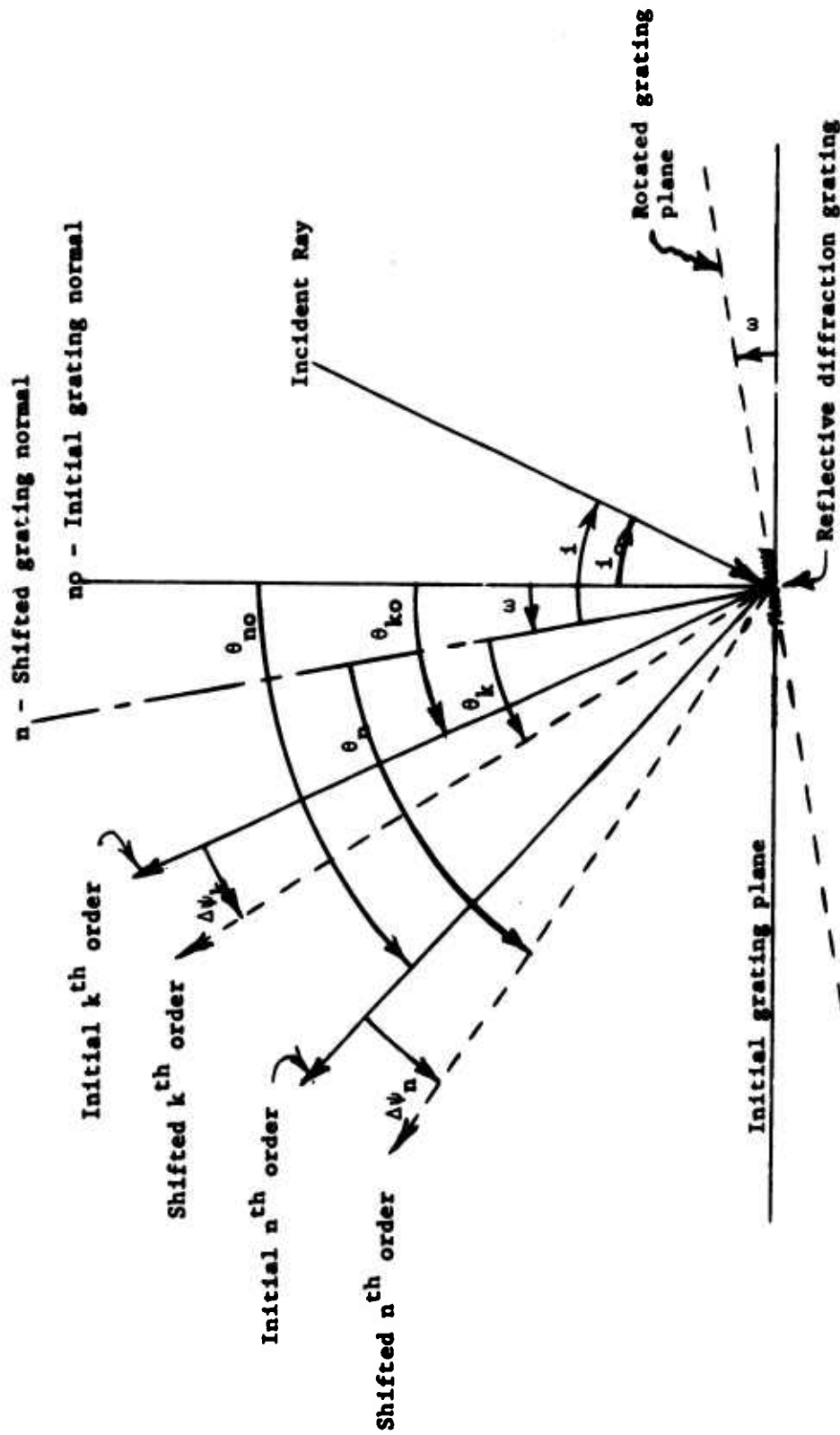
Figure 2.2.2 Diffraction Pattern Shift due to Grating
Surface Rotation and Normal Strain

Applying the trigonometric identities

$$\sin (x \pm y) = \sin x \cos y \pm \cos x \cos y \qquad (2.2.12)$$

to equation (2.2.11) gives

$$n \lambda m = \sin (\theta_{no} + \Delta \psi_n) \cos \omega - \cos (\theta_{no} + \Delta \psi_n) \sin \omega$$

$$- \sin i_o \cos \omega - \cos i_o \sin \omega \qquad (2.2.13)$$

Collecting terms in (2.2.13)

$$n \lambda m = [\sin (\theta_{no} + \Delta \psi_n) - \sin i_o] \cos \omega$$

$$- [\cos (\theta_{no} + \Delta \psi_n) + \cos i_o] \sin \omega \qquad (2.2.14)$$

or

$$n \lambda m = (\sin \alpha - \sin i_o) \cos \omega - (\cos \alpha + \cos i_o) \sin \omega \qquad (2.2.15)$$

where

$$\alpha = \theta_{no} + \Delta \psi_n \quad . \qquad (2.2.16)$$

Similarly for the kth order

$$k \lambda m = (\sin \beta - \sin i_o) \cos \omega - (\cos \beta + \cos i_o) \sin \omega \qquad (2.2.17)$$

where

$$\beta = \theta_{ko} + \Delta \psi_k \quad . \qquad (2.2.18)$$

Dividing equation (2.2.15) by $n\lambda$, equation (2.2.17) by $k\lambda$ and equating the results gives

$$\frac{1}{n\lambda} [(\sin \alpha - \sin i_o) \cos \omega - (\cos \alpha + \cos i_o) \sin \omega] =$$

$$\frac{1}{k\lambda} [\sin \beta - \sin i_o) \cos \omega - (\cos \beta + \cos i_o) \sin \omega] \quad . \qquad (2.2.19)$$

Collecting terms in equation (2.2.19) and dividing through by cos ω gives

$$\tan \omega = \frac{k(\sin \alpha - \sin i_o) - n(\sin \beta - \sin i_o)}{k(\cos \alpha + \cos i_o) - n(\cos \beta + \cos i_o)}$$

where   (2.2.20)

$$\alpha = \theta_{no} + \Delta\psi_n$$

$$\beta = \theta_{ko} + \Delta\psi_k$$

Now, equations (2.2.20), (2.2.15), and (2.2.3) provide a usable set of diffraction-strain relationships in terms of the initially known quantities

m_o = the initial line density of the grating

i_o = the initial angle of incidence

θ_{ko}, θ_{no} = the initial diffraction angles of the kth and n^{th} orders respectively

and the measurable quantities

$\Delta\psi_k$, $\Delta\psi_n$ = the angular shifts of the kth and n^{th} orders respectively, positive counterclockwise.

It should be noted that the major assumptions contained in the derivation were that during deformation the plane of the incident colli-mated light remains normal to lines of the grating and that surface rotation of the grating is confined to that component about an axis parallel to the lines of the grating; however, within these assumptions, the above expressions are completely general with respect to selecting an initial angle of incidence and the selection of active orders to be observed. Special cases of the above may be found in the publications

of Bell (19), Liddell (26), and Liddell et. al. (21). Various other cases involving different incident light plane orientations for single gratings as well as diffraction-strain relationships for crossed gratings (two single gratings superimposed with lines crossed forming a grid) are presented by Blake (27).

3 Development of a Hypervelocity Impact Strain Measurement System

3.1 Introduction

The discussions and descriptions contained in this chapter pertain to the development of a hypo- and hypervelocity impact strain measurement system capable of measuring the large deformations and deformation rates of rods experiencing axial impact at velocities greater than twice the sound speed of the rods. A description of the experimental problem and discussion of the application of the diffraction grating technique to this problem are intended to provide clarity as to the requirements of such a system.

The major components of the system (accelerator and instrumentation for velocity measurements, illuminator, and the recording system) are then described and discussed as solutions to those design requirements. Subsequent discussions of the experimental procedures are intended to provide the specifics of producing, recording and reducing data from the axial hypo- and hypervelocity impact of rods.

3.1.1 The Experimental Problem

The impact problem under consideration is the axial impact of a free flight projectile with a target rod which is initially at rest. Both projectile and target are rods of circular cross section, with the same diameter, and of the same material. If the projectile (impact) velocity is greater than twice the elastic wave velocity of the material, the impact is called hypervelocity. Velocities in this regime but less than this value are referred to as hypovelocity.

In order to evaluate the scaling law of late-stage equivalence $(L_o V_o^\alpha = L_1 V_1^\alpha)$, it is necessary that the projectiles be accelerated to the requisite speeds and that these (impact velocities) be known as initial conditions to characterize the resulting deformations.

At selected axial positions on the outer circumference of the target rods, longitudinal deformation histories are to be recorded using a diffraction grating technique. From these records, quantitative information about the axial strain histories is to be determined for a group of target rods experiencing different impact conditions (values of L_o and V_o) and compared to test for the existence of late-stage equivalence. Late-stage existence is assumed to exist if the families of strain histories for two different impacts are identical.

3.1.2 Application of the Diffraction-Strain in Relationships to the Experimental Problem

As was summarized in the previous chapter (2.2), the major configurational assumptions contained in the derivations were that the plane of the incident light should remain normal to the lines of the grating and hence the only component of surface rotation permitted is about an axis parallel to the lines of the grating. Satisfaction of those requirements permits one to use equations (2.2.20), (2.2.15), and (2.2.3) for the computation of surface strain normal to the lines of the grating.

The symmetrical deformation resulting from the axial impact of rods provides natural satisfaction of those requirements for the following orientation of grating and incident light plane. If as shown in Figure 3.1.1, the lines of the grating are normal to the axis of the rod such that all rotation of the grating surface is about an axis
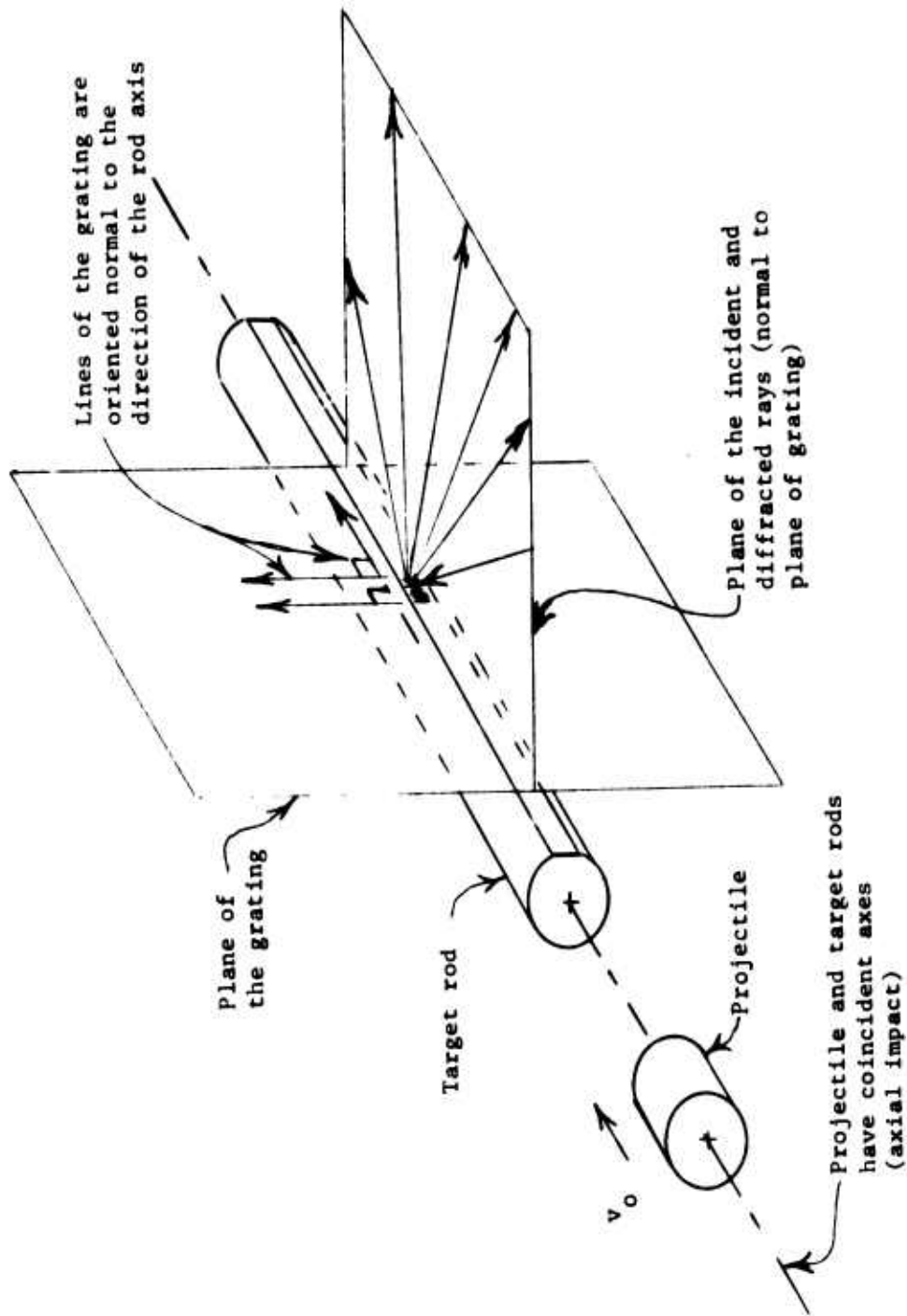
Figure 3.1.1 Orientation of the reflective grating and light plane
for planar motion of the diffracted rays during
axial impact.

parallel to the lines of the grating and the incident light lies in the plane normal to the lines of the grating, then the incident ray, the reflected ray, and the diffracted rays are coplanar and the motion of all rays during deformation of the grating is confined to this plane. The following diffraction grating strain measurement technique is based upon tracking the planar motion of two of those rays from the time of impact and the assumption that any recorded angular motion is due to either rotation or deformation of the grating.

3.2 The Experimental System

Based on the comments of the previous sections, the basic requirements for a diffraction grating strain measurement system used to determine axial surface strains during axial hypo- and hypervelocity impact can be stated as follows:

1) To provide a means of accelerating the projectile to hypo- and hypervelocity speeds and measuring those velocities,

2) To provide an optically clean path for incident and diffracted rays free of gas and flying debris,

3) To provide a collimated monochromatic light source, of sufficient intensity for dynamic recording, which illuminates the grating at the proper time,

and 4) To provide a means of tracking the planar movement of two of the diffracted rays during deformation from the onset of impact.

3.2.1 Projectile Acceleration and Velocity Measurement.

The projectile was accelerated to hypo- and hypervelocity speeds by the two stage accelerated reservoir gun shown in Figure 3.2.1. This
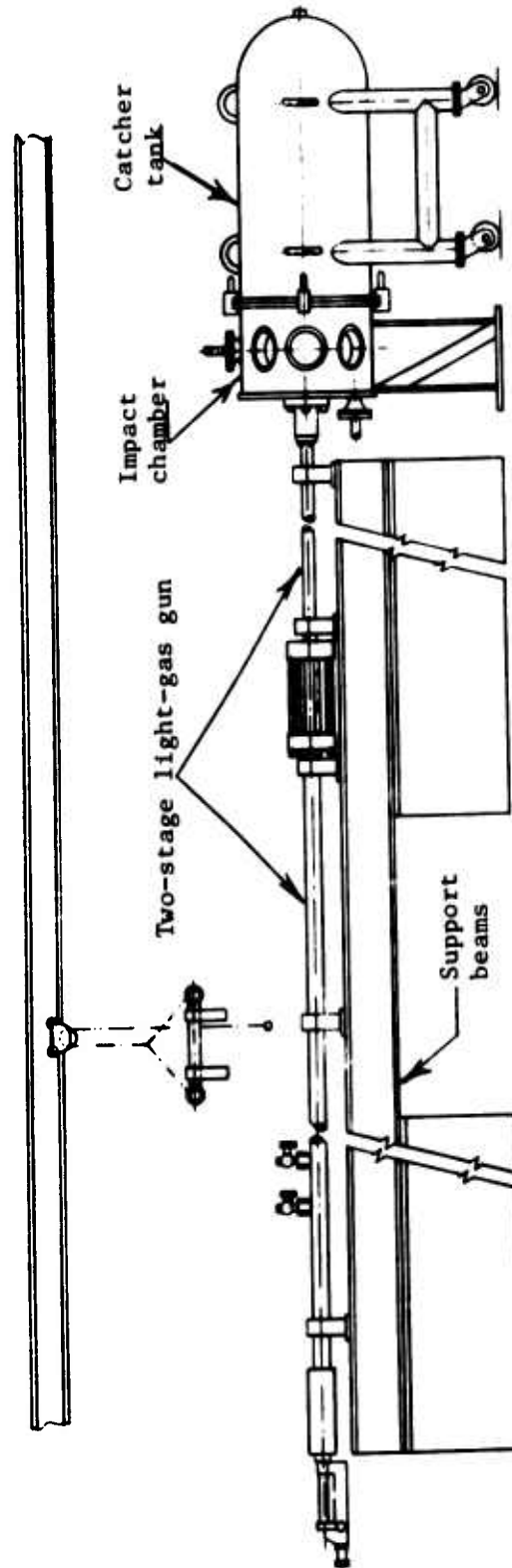
Figure 3.2.1 Two-stage light-gas gun system used to attain hypo and hypervelocity speeds.

is a system designed for this laboratory which consists of the gun, an impact chamber in which to make measurements, and a catcher tank to stop the projectile and target debris. The basic principle of operation is that an explosively driven heavy piston is used to compress a gas column which is in turn used to accelerate a light projectile to the desired velocity. Selection of piston weight, powder charge and initial gas pressures was based upon the analysis of John Curtis (28). Discrete values of these variables required for the acceleration of projectiles having mass of from 5 to 10 grams, to velocities of 8,000 to 20,000 feet per second can be found in a previous publication (29). Also contained in this report are details as to the care and firing of this two-stage light-gas gun.

The velocity of the projectile at impact was determined by a pre-calibration of the gun. Pre-calibration was accomplished by firing the projectile through two breakwires of known separation and using an electronic counter to record the time elapsed between breaks. Specifically the physical configuration was that of two .010 inch diameter lacquer coated copper wires stretched over the ends of a steel tube with insulated ends (Figure 3.2.2) 15.026 inch long which was placed in axial concentricity with the bore of the launch tube by using a mandrel.

The simple electronic circuit shown in Figure 3.2.3 provided essentially noise-free rising emf signals to a Model 6380 Beckman counter for a time interval count with error of only ± .1 microsecond. The reason for choosing this circuit rather than an even simpler circuit of placing the wires as a direct short across the voltage was that the driver gas immediately behind the projectile was found to be somewhat
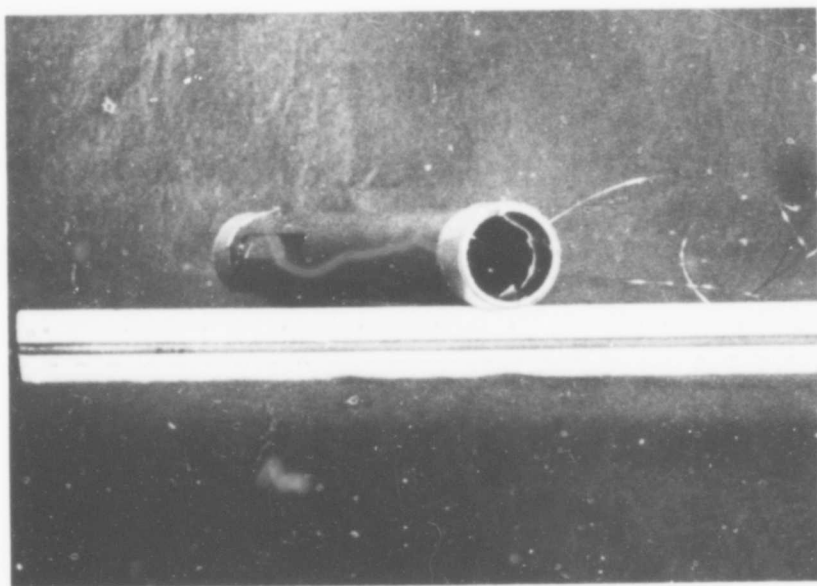
Figure 3.2.2 Breakwire tube used for
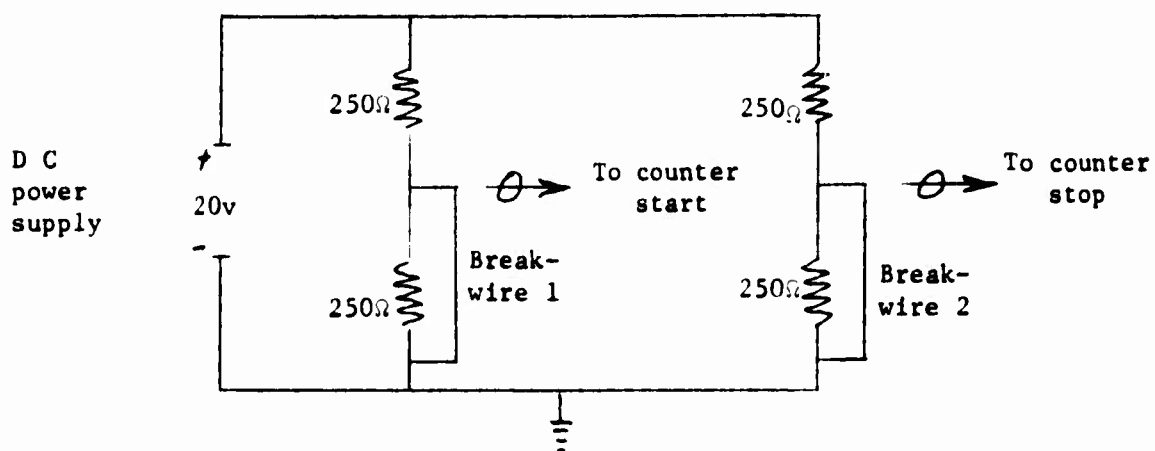velocity calibrations.

Figure 3.2.3 Schematic of circuit for measuring time elapsed between breaking of wires in velocity calibration tests.

conductive. The circuit of Figure 3.2.3 provides a continuous path for current flow after the breakwire is broken and serves as a "short" to the higher resistance path of the driver gas. Subsequent application of the above system resulted in trouble free velocity measurements for over thirty firings.

3.2.2 Optically Clean Recording Environment

Although the operation of the light-gas gun requires that the launch tube, impact chamber and catcher tank initially be evacuated to reduce air friction on the projectile, there remain two sources of pollutants to the recording environment. The first and most problematic is the gas which drives the projectile. After the projectile leaves the launch tube, the gas column which is behind the projectile is free to expand and enter the path of the incident and diffracted rays and produce non-predictable Schlerien type diffraction of these rays. This was prevented by the use of a baffle system to slow the gases and keep the optical path clean during the time of measurement. The system is shown in Figure 3.2.4 and consists of a primary deflector, which is attached to the end of the launch tube so as to absorb the initial loading of the high pressure gases, and secondary deflectors to serve as guides to deflect the gases above and below the recording platform. The early arrival (approximately 200 micro-seconds before impact) of gases probably blown past the projectile while in the launch tube necessitated additional shielding in the form of a housing for the light path (also shown in Figure 3.2.4) using the recording platform as a base.

This system provided a sufficient time delay from gas interference for the bulk of the expanding gas column; however, due to the proximity
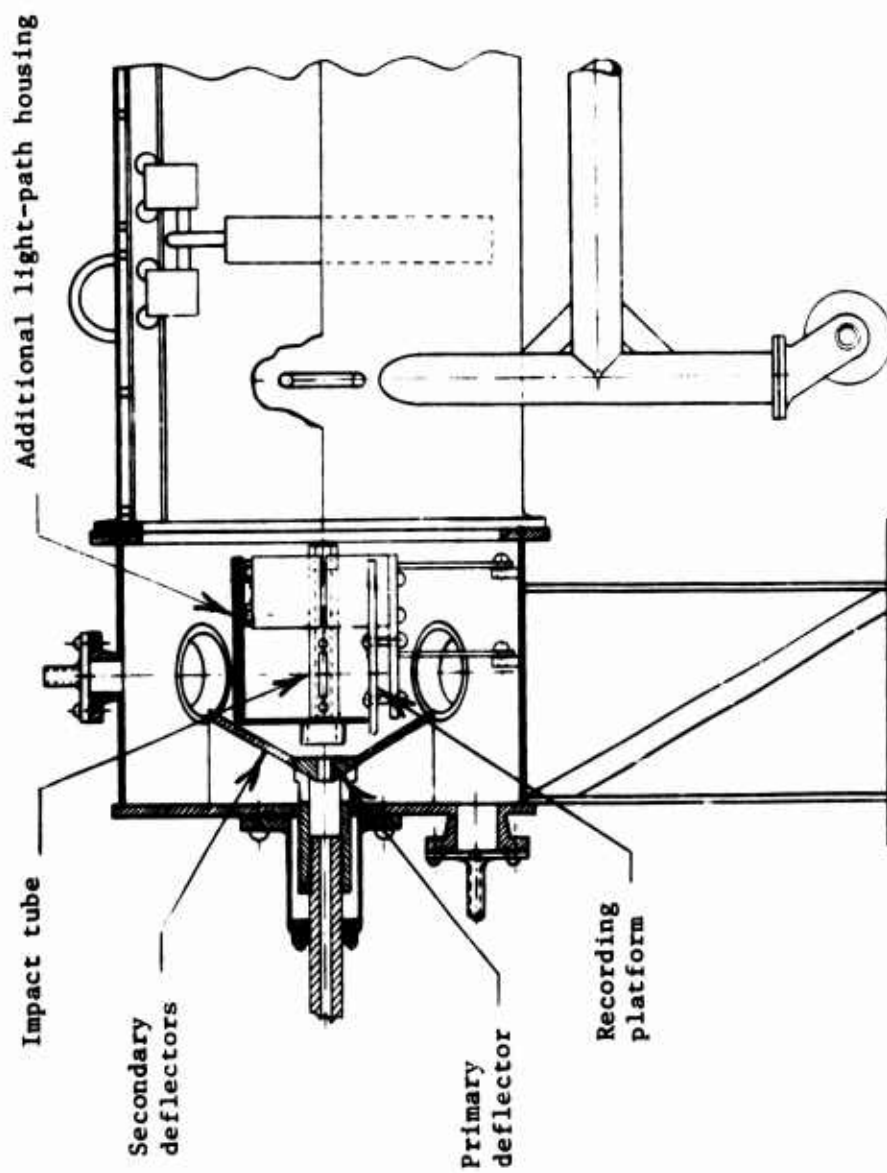
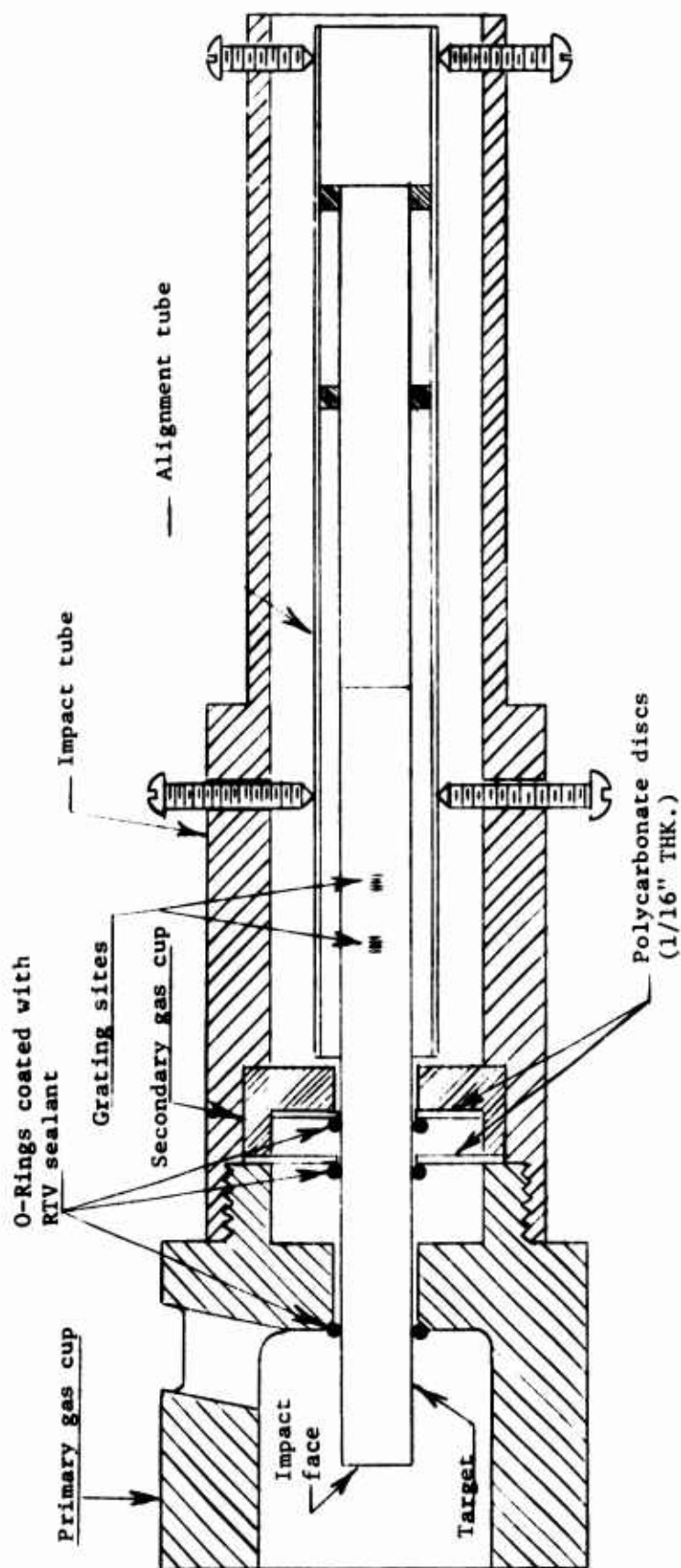Figure 3.2.4 Baffle systems used to create an optically clean environment.

Figure 3.2.5 Cutaway view of impact tube showing interior gas and debris baffles.

of the impact site to the end of the launch tube (chosen so as to reduce the possibility of projectile tilt), there remained a quantity of gas immediately behind the projectile which followed the projectile through the primary baffle and which served to pollute the grating site. The solution to this problem and the additional problem of pollutants from the molten flying debris created by the hypervelocity impact is shown by the cutaway view of the impact tube of Figure 3.2.5. This assembly of steel and polycarbonate baffles (to stop debris), with RTV coated o-ring seals around the target (to delay gas passage) provided normal recording times of over 200 microseconds after impact.

3.2.3 Light Source

The monochromatic collimated light source was provided by a Korad Model K-1C JR pulsed ruby laser operating in the normal mode. Additional collimation and increased light field width, to permit extended recording during target translation, were attained by directing the laser through a beam spreader described in previous work by Liddell (19,24). This resulted in a collimated light field approximately 1 1/2 inch in width with a measured beam angle of .15 milliradians (24).

Although the additional requirement of sufficiency of intensity for dynamic recording is provided by the 8 joule rated pulsed ruby laser, the pulsing characteristic presented problems in initial alignment with respect to the grating surface and in synchronization of the 1 millisecond pulse width with the arrival of the projectile at the impact site. The solution to the first problem was to direct the beam of a continuous helium neon laser (15 milliwatt/rated) through the ruby laser-beam spreader system (19,24) such that the continuous beam was coincident with the light emitted
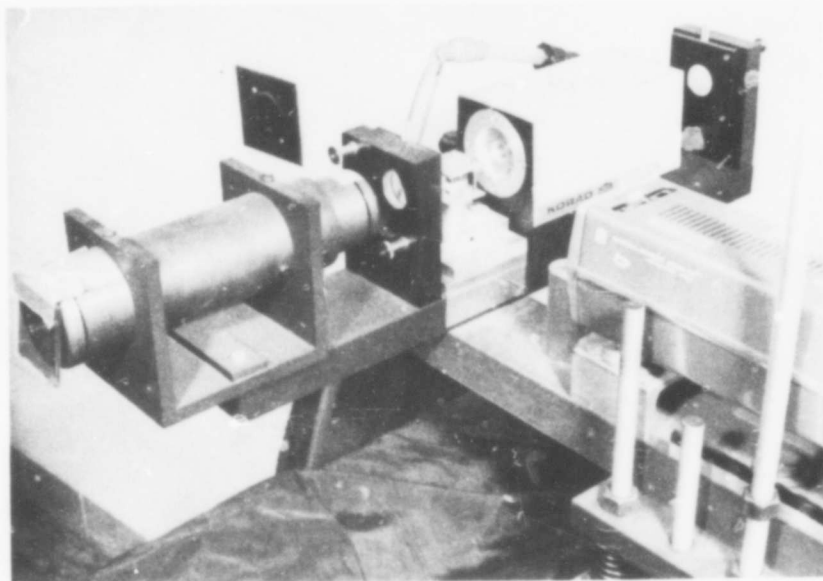
Figure 3.2.6   The illuminator assembly consisting of the
Korad ruby laser, the beam spreader, the
continuous alignment laser, and the removable
alignment mirror.

by this system. Measurements indicated this angular deviation from
collinearity was .44 milliradins (24). For convenience of use a dowel-
located removable alignment mirror (shown in Figure 3.2.6) was located
in the laser cavity to direct this alignment beam.

The problem of synchronizing the laser pulse with the arrival of
the transient deformations at the grating site was solved by providing
a reliable early trigger for the laser control circuitry. This trigger
signal originated from an electrical resistance strain gage placed on
the launch tube to sense the passage of the projectile and provide an
..iectrical disturbance to fire the laser.

The gage was positioned far enough upstream of the impact site so
that the projectile transit time (from the gage site to the impact site)
would encompass the required 600 μ sec rise time of the laser for all
anticipated velocity levels. The expected change in projectile transit
times (encountered when moving to a new velocity level) were accounted
for by first directing the strain gage signal into a pulse delay generator
to trigger the laser. This extremely versatile system was found to be
quite reliable for all velocity levels used in the experiments.

3.2.4 The Recording System

As was discussed in an earlier section (3.1.2), the diffraction
grating strain measurement technique is based upon tracking the angular
motion of the diffracted rays which result from deformation and rotation
of the grating. This tracking was achieved optically in the present
study by using a high speed camera to photograph the transient motions of
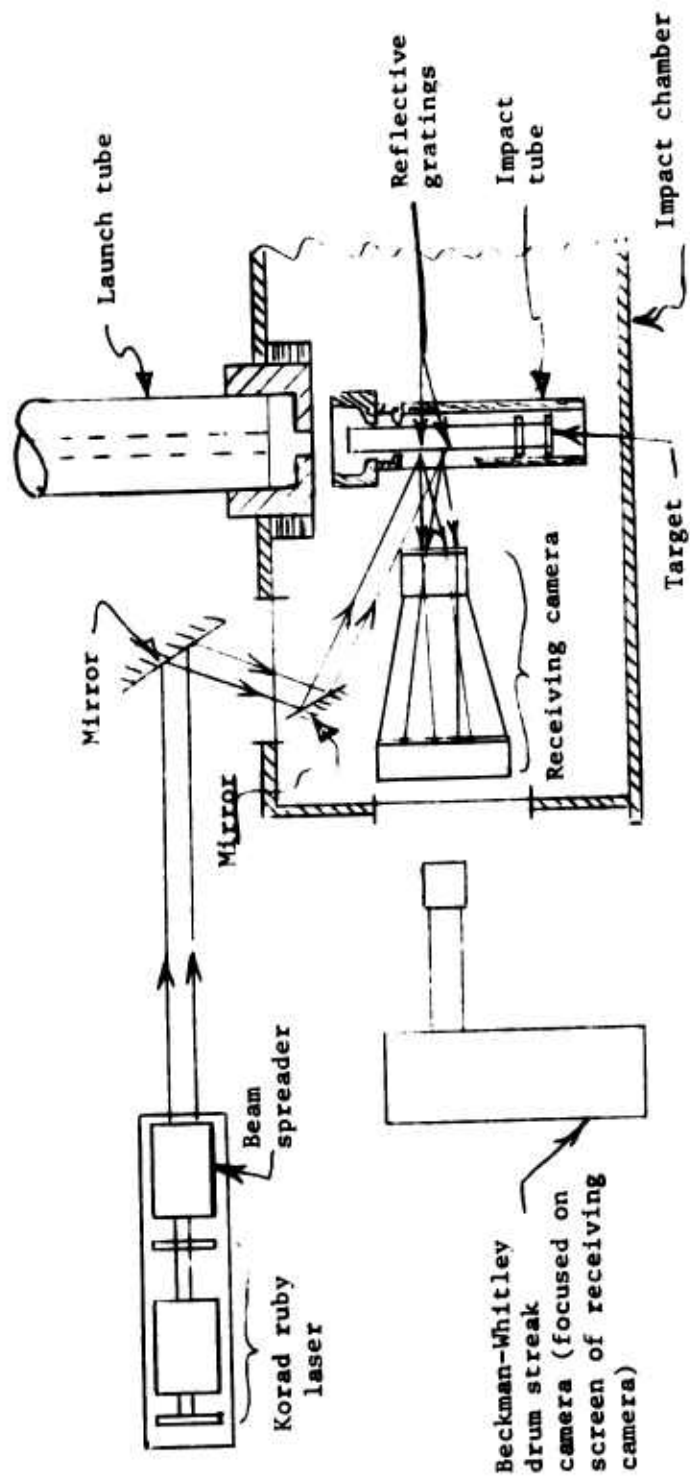the rays during impact.

Figure 3.2.7 Sketch of the optical configuration for illumination of the reflective gratings and recording of the diffracted rays.

As indicated in Figure 3.2.7, the recording system consists of two components. The diffracted rays first enter a "filmless" receiving camera with a focusing screen placed in the focal plane of the lens. This receiving camera is placed as close as possible to the grating sites and provides the capability of recording large angle changes. Directly behind the receiving camera is a Beckman and Whitley model 318 drum camera which is focused on the focusing screen of the receiving camera. Since the configuration of Figure 3.2.7 conforms to the requisites of Chapter 2 and Section 3.1.2, the initial positions of the diffracted rays are coplanar and the motion of these rays during deformation is confined to this plane. The recording concept of the streak camera is based upon using a rotating drum to streak the film through this image plane in a direction normal to the plane of motion of the rays. It thus provides a time versus angular position record of the required (two) rays as shown in Figure 3.2.8.

Due to the lack of a fast response shutter for the Beckman-Whitley streak camera, the experiments were run with the camera in an "ever-ready" mode with the mechanical shutter open for the duration of the time required to complete a firing. A 6943 Å interference filter (equal to the wavelength of the active orders) was placed over the lens of the streak camera to control background lighting (from the muzzle flash, from the ignition flash lamp of the ruby laser, and from room lighting). Exposures were effected through the use of neutral density filters and f stop settings on the Beckman-Whitley camera.

Since the Beckman-Whitley streak camera was operated in the "ever-ready" mode, the film record started recording ray angular positions from the time that the ruby laser started initiation of the laser pulse. As shown in Figure 3.2.8, the resulting film record consists of

initially straight "rows" of dots separated in the time direction by physical spacings corresponding to the discrete burst characteristics of this particular laser pulse. This is due to the fact that a ruby pulsed laser does not emit a continuous burst of long duration but rather a set of discrete bursts of random time separation.

Hence, it was decided to monitor the light pulse for each experiment and use the random burst characteristics to "fingerprint" an impact time. Monitoring was accomplished by directing a reflected ray off one of the optical ports onto a fast response photo-transistor circuit shown in Figure 3.2.9. This signal was recorded on a 556 Techtronics oscilloscope with the sweep triggered by a simple electronic impact switch.

The impact switch consisted of two 0.010 inch diameter lacquer-insulated copper wires crossed over the nose of the target and connected across the terminals of a 12 volt dry cell battery. The impact of the projectile against the target served to crush the wires together and close the switch of the circuit.

Shown in Figure 3.2.10 is a typical laser pulse record used for identifying the impact time. The bottom trace of the oscilloscope record (started by the impact switch) shows the relative intensities and time spacings of the laser spikes immediately following impact. The top and middle traces (started by the previously discussed launch tube signal) show the complete laser pulse (top) and impact trigger signal (middle). Comparison of these two traces indicated the time position of the impact switch within the complete laser pulse and in many cases this added information served to simplify the matchup of the bottom line of the oscilloscope record with the accompanying active order record. The distinct variations in intensities and time spacings of the individual laser spikes shown in Figure 3.2.10 generally facilitated the matchups and this technique
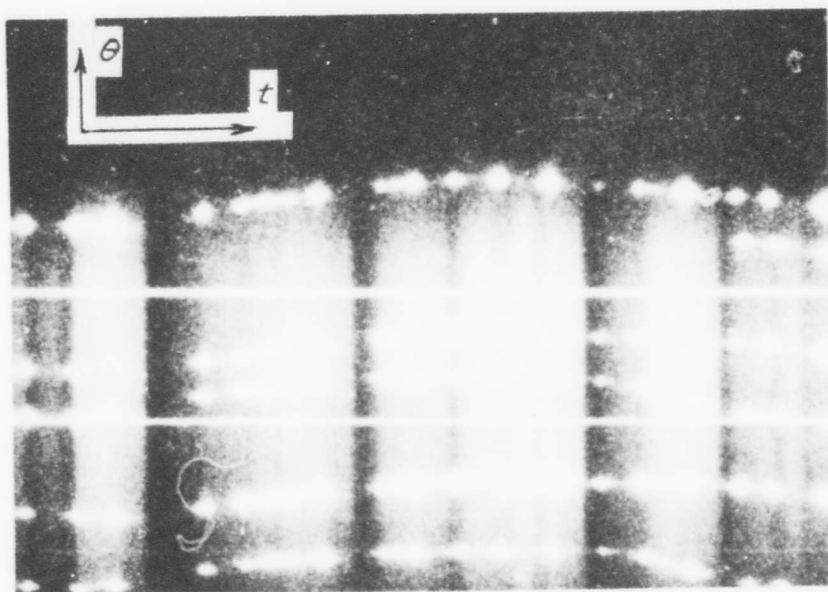
Figure 3.2.8 Print of typical Beckman-Whitley film record
containing the angular displacement – time
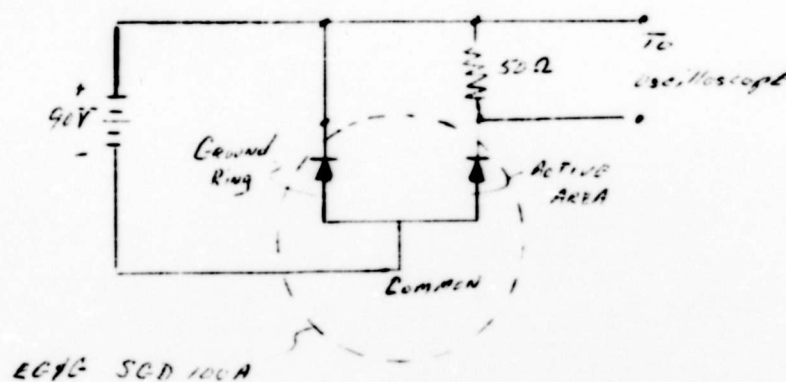information for the diffracted orders.

Figure 3.2.9 Fast response photodiode circuit used to monitor the laser pulse.
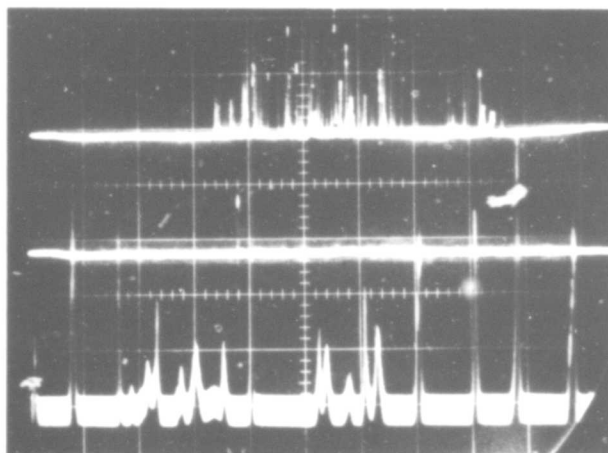

Figure 3.2.10 Typical oscilloscope record used with film record of diffracted rays to determine impact time.

quite successfully determined impact times within 1 microsecond.

Although the filmless receiving camera was constructed by mounting a ground glass screen in the focal plane of an excellent quality Kodak Aero-Ektar, f/2.5, 7 inch focal length lens, the assembly exhibited a slight non-linearity in transfer characteristics. For simplicity of data reduction, it was hoped that any angular change of a collimated ray entering the lens would be relayed as a proportional change in dot position on the focusing screen for all angular changes; however, it was found that the proportional change could vary by 6% depending upon the initial angular orientation of the entering ray with respect to the optic axis of the lens. Hence, a calibration was performed to account for this non-linearity by mapping the field of the camera.

This mapping simulated real measurement conditions by placing a sextant mirror at the approximate position of a grating location during the experiment ($\simeq$ 6 1/2 inches from the lens center) and sweeping a collimated ray across the face of the lens. Corresponding dot positions on the focusing screen were located using a vernier x-y microscope. The resulting plots of angular position of the entering ray with respect to the lens optic axis versus dot position on the focusing screen were used to correct indicated angular shifts taken from the film records.

3.3 Target Preparation, Support and Alignment

The procedures involved in target preparation are nearly identical to those described by Liddell (24) and may be summarized briefly as follows:

1) polycarbonate (Lexan) rod in the as-received condition is machine finished to a diameter of .743 inches, then cut to the desired length and the ends faced.

2) standard metallographic polishing procedures are used to create an optical flat 1/8 inch wide and parallel to the axis of the rod.

3) the Douglas grating machine is used to make gratings with the lines perpendicular to the rod axis at the desired axial locations. The line densities of the gratings used in this investigation were nominally 5000 lines per inch. This value of m_o was chosen to permit recording of at least two active orders per grating with the single receiving camera recording system shown in Figure 3.2.7. These grating sites are then vacuum plated with aluminum to a 5 kilocycle thickness to increase the intensity of orders.

4) a black felt pen is then used to paint off the starting and ending grooves of the grating (to improve grating quality since these usually have irregular spacing) as well as the surrounding aluminum coated target area (to reduce background illumination).

5) this rod is then attached to the front of an equal diameter Lexan support rod by forming a methylene chloride bond. This junction is performed with the two rods placed in a V-block configuration to achieve axial alignment. Measurements indicate that eccentricity is less than .001 inch.

The procedure, described in item 5, of attaching a front rod complete with gratings to a like material, same diameter support rod
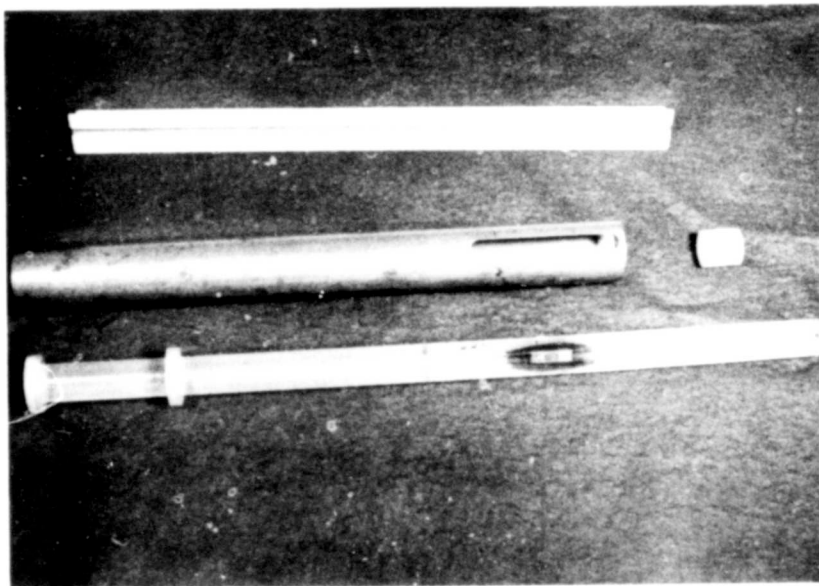
Figure 3.3.1 Samples of the alignment tubes, projectiles and
targets used in the investigation.

permits one to construct a long target rod (Figure 3.3.1) with the grating site a long distance from both the impact site (5-6 inches required by the steel baffles) and the influence of the support rings. Initial curvature of the rod in the as-received condition and size limitations of the metallographic equipment prevented manufacturing the target rod from one continuous section; however, the methylene chloride bonding technique is reported (30) to provide a tensile bond strength of 9,000 - 10,000 psi which is approximately the tensile yield strength of the polycarbonate and it was decided that this would provide a joint of suitable integrity since the measurement of compressive strains was anticipated and all such junctions were made downstream of the measurement sites.

Target support is achieved through the use of Lexan support rings attached to the tail end of the support rod as shown in Figure 3.3.1. These rings are 1/8 inch thick and separated axially 3 inches. The outer diameter of these rings is turned to provide a sliding fit in an alignment tube which can be used for positioning. This alignment tube, made from seamless mechanical steel tubing, is placed in the impact tube, (Figure 3.2.5) concentric with the bore axis of the launch tube by using a mandrel.

3.4 Evaluation of Initial Parameters

As noted in Chapter 2, the application of the diffraction-strain relationships assumes " -priori" knowledge of the initial values of the line density of the grating m_o, the angle of incidence i_o, and the initial diffraction angles of the two active orders being recorded

(θ_{ko} and θ_{no}). The following simple procedures were used to ascertain these values.

The evaluation of the initial line density, m_o, was accomplished by illumination of the grating at normal incidence with a laser, the measurement of the included angle between two of the diffracted rays and the application of Equation (2.2.4). Specifically, the continuous beam of a 1.5 milliwatt Spectra Physics Model 132 laser was aligned normal to the surface of the grating by directing the collimated incident ray through a pinhole and orienting the grating such that the reflected ray passed back through the pinhole. The included angle between two of the symmetrically positioned diffracted rays (say the + and the − 4) was measured by again using a pinhole technique. A pinhole was positioned such that one of the diffracted rays could pass through and a translatable sextant mounted mirror was used to reflect the ray back through the pinhole. The same procedure was then followed for the second ray using the change in angle of the sextant to provide the required angle. The uncertainty of this technique was estimated to be ± 2 minutes. The angle between the surface normal and the diffracted ray, θ_{no}, the angle of incidence ($i_o = o$), the wavelength of the light (6328 Å) and the order number, n, was then placed in Equation (2.2.4) to compute the initial line density, m_o.

Alignment of the laser for a known non-normal angle of incidence (i_o) was accomplished by first locating the grating normal with a small cw laser and the pinhole technique described above. Then the ruby laser was oriented such that one of the diffracted orders from its continuous alignment beam (say the − 4 order) was directed through the pinhole.

This positioning of one of the diffracted orders normal to the grating surface ($\theta_n = 0$) and the previously determined, m_o, permits application of Equation (2.2.4) for computation of i_o, the initial angle of incidence.

The presently known information, i_o and m_o, then permits one to compute with Equation (2.2.4) the initial diffraction angles, θ_{no} and θ_{ko}, for illumination by the ruby laser ($\lambda = 6943$ angstroms).

3.5 Data Reduction

With the initial parameters evaluated by the techniques of the previous section, there remains only the determination of the angular shifts $\Delta\psi_k$ and $\Delta\psi_n$ of the diffracted k and n rays from the Beckman-Whitley film record. Note that in addition to the rows of dots shown in Figure 3.3.8, there are also continuous straight lines. These lines are put on the film immediately prior to firing the system by illuminating the grating sites with the continuous alignment laser and streaking the images of the diffracted orders with the gratings experiencing no strain.

The purpose of these lines is twofold:

1) Since they are put on with the camera at speed and the film is held in place by the centrifugal forces created by the rotating drum, they serve as reference streaks to accurately define the time direction on the film.

2) Since the angular separation of the rays is known (it can be calculated using i_o, m_o, and $\lambda = 6328$ Å to put in Equation 2.2.4) they serve to define the magnification factor from the focal plane of the receiving camera to the film plane of the Beckman-Whitley camera.

The film record is placed in a vernier x-y microscope and the reference streaks are used to align the film with one axis of the microscope. Starting with the initial dots, the displacements of the diffracted orders in the time and angular position directions are determined. This data, along with the initial parameters and all other system characteristics is put in a computer program to use the equations of Chapter 2 and compute strain-time values for each grating site referenced to the time the ruby laser initiated pulsing. Then using the previously discussed match-up technique, the impact time is determined and the time values for each data point are adjusted so that the resulting strain histories are now referenced to the time of impact.

An uncertainty analysis (31) was carried out for these measurement techniques and this configuration which indicated that the dominant factor affecting the strain uncertainty was the initial angular separation of the two diffracted orders being used to determine the strain. Generally it was found that a large initial separation of the diffracted rays produced a small strain uncertainty and care was taken to select the two recorded diffracted rays having the maximum initial angular separation. For the optical configuration and grating line densities used in these investigations, typically this meant using alternate orders (k and k+2). The strain uncertainty associated with these measurements was computed to be 0.002 in/in. In some cases, when the diffracted rays of two gratings were being recorded, only adjacent orders were recorded for one of the grating sites and the strain uncertainty associated with these measurements was computed to be about

0.0045 in/in. The agreement between duplicate experiments, however, indicated that these values are slightly conservative.

3.6 Summary

It is noted that the basic concept of utilizing a receiving camera and an in-line streaking camera to record the transient motion of the rays is the same as that used by Liddell (24) in his investigations at much lower impact velocities. Indeed, the physical components were a part of the system used by him at this laboratory; however, the space requirements and optical port locations of the two-stage light-gas gun impact chamber eliminated the use of his reliable and accurate, normal-incidence, symmetrical-recording configuration.

Faced with these limitations, the new configuration using non-normal incidence and a single set of cameras as shown in Figure 3.2.7 (along with the resulting different data reduction equations) was developed to use with this system. The system was found to be quite usable in the measurement of strains in polycarbonate rods experiencing hypo- and hypervelocity impact. Due to the required gas shielding, axial measurement positions were limited to those far enough downstream of the impact site to be in the strength-affected zones, yet strains of 5% in this region were easily recorded.

The configuration was found to be quite usable in the simultaneous recording of information from two grating sites separated by an axial distance of one-half inch. It is felt that this feature would be quite attractive to those involved in the determination of large amplitude wave propagation speeds.

4 Experimental Results and Conclusions

4.1 Introduction

Within the limitations discussed in Chapter 1, Walsh's late-stage equivalence principle predicts that two separate and different projectile-target impacts will produce identical target deformations if the initial conditions of the impacts satisfy the simple relationship $L_o V_o^\alpha = L_1 V_1^\alpha$ (where L_o and L_1 represent characteristic dimensions of the projectiles and V_o and V_1 are the respective projectile impact velocities). For the axisymmetric case of projectiles of various shapes normal impacting a semi-infinite solid target the value of α is equal to 0.58. For the extreme projectile shape (a thin slab having infinite lateral dimensions) producing the one-dimensional strain state in the target, the value of α appears to be dependent upon material properties yet is bounded by the values 1 and 2. The results contained in this chapter were obtained as a test of the validity of this principle for a new target configuration.

Using the system described in Chapter 3, short, cylindrical, poly-carbonate projectiles were accelerated to hypo- and hypervelocity speeds to axially impact against initially-stationary, like-material, equal diameter (0.743 in.), long (> 21 diameters) target rods. In order to maximize the quantity of information gathered from each experiment, axial surface strain measurements of the resulting transient deformations were simultaneously recorded from two axial positions on the target rods. Descriptions and illustrations of the quality of these results are found in the next section to aid in evaluations of the comparisons made in subsequent sections.

In the absence of analytical guidance for this particular projectile-target configuration, the test procedure was to first collect strain histories for a reference value of L_o and V_o and then to search for late-stage equivalence by moving to a new velocity level and scan the effect of changing projectile lengths. The results of this investigation and a subsequent test of its indicated equivalence are shown in Sections 4.3 and 4.4.

Subsequent discussions pertain to the generality of the results and the conclusions of the investigation (4.5 and 4.6).

4.2 Reproducibility of the Strain-time Data

In any experimental investigation, the factors primarily affecting the reliability of the experimental results are the sensitivity of the measurement system and the capability of the test apparatus to exactly reproduce the test conditions in duplicate experiments. As an evaluation of the influence of these parameters on the experimental results, let us examine the comparison plots (Figures 4.2.1 and 4.2.2) of the individual strain-time curves determined for the reference case (chosen since it has the most duplication experiments).

The results shown in Figures 4.2.1 and 4.2.2 were obtained from three separate (but hopefully duplicate) experiments by the aforementioned simultaneous recording of diffracted rays from the two grating sites on the target rods. The influence of the system sensitivity is indicated by a comparison of the fit of the results from the three experiments, as well as the smoothness of the individual curves shown at each grating site. Of significance is the fact that the curves of grating site 2 were reduced from the recorded motion of alternate diffracted orders (say k and k+2)
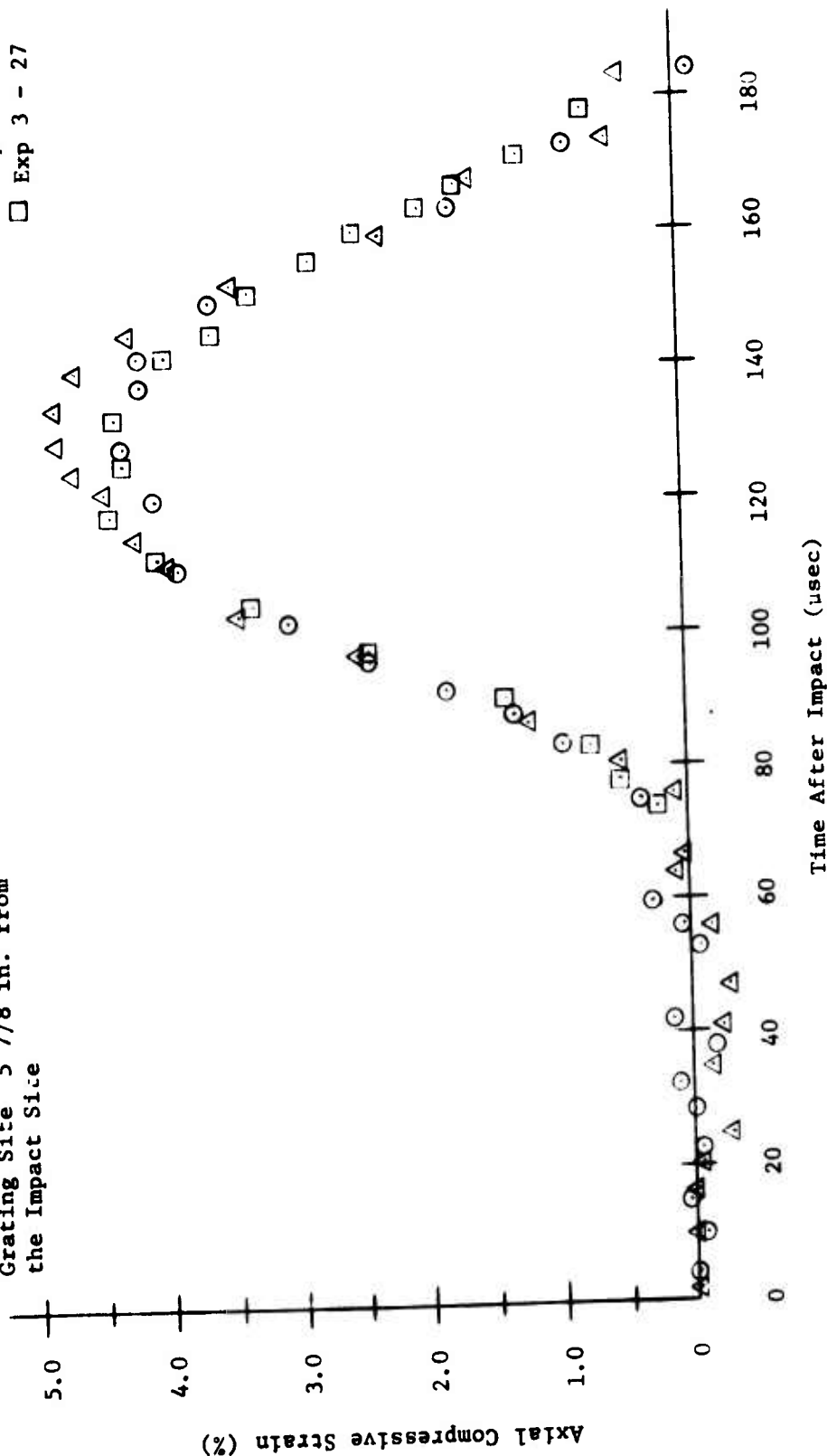
Figure 4.2.1 Strain histories at grating site 2 as determined from the three
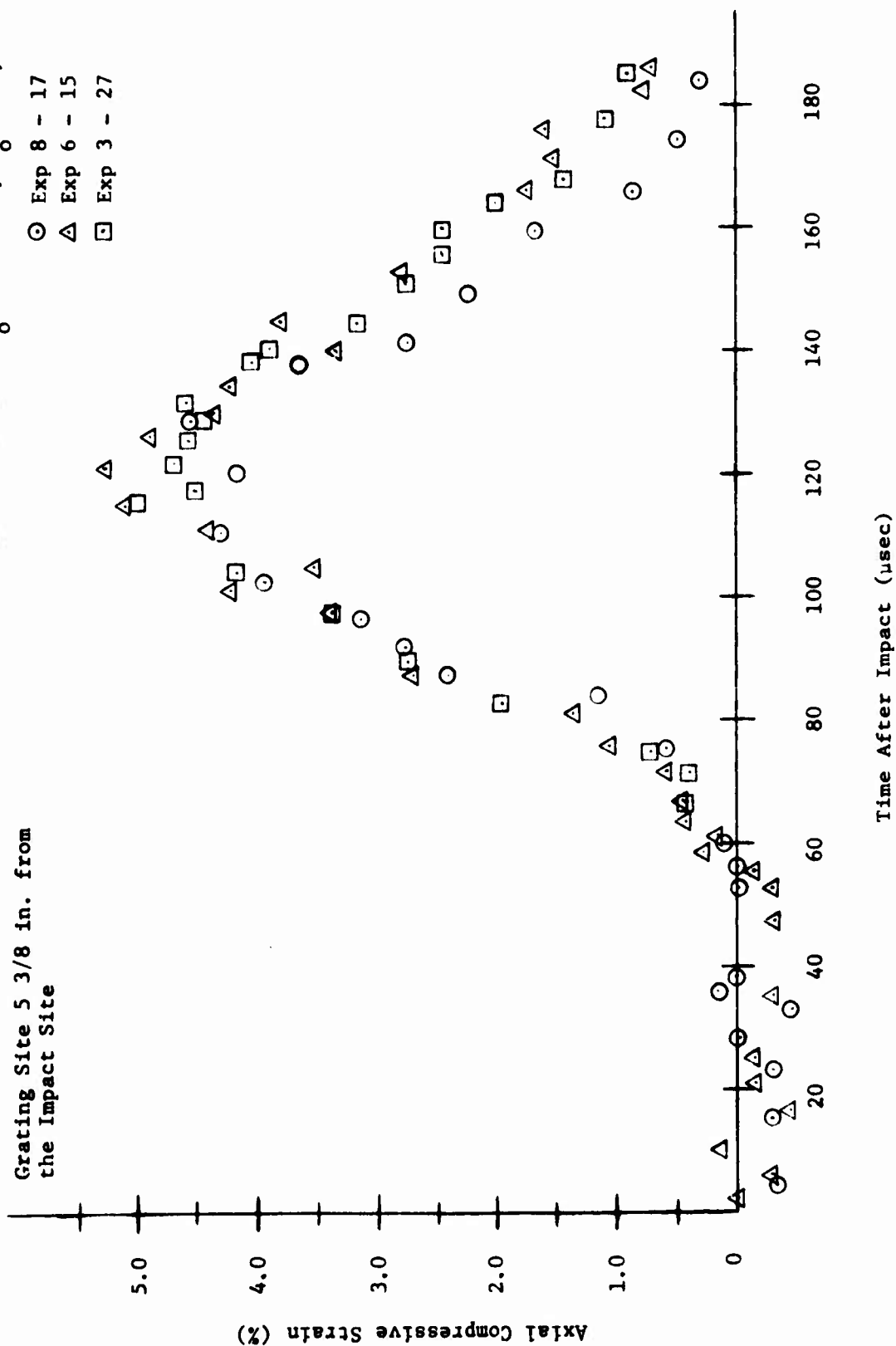experiments for the reference case.

Figure 4.2.2 Strain histories at grating site 1 as determined from the three experiments for the reference case.

having a larger initial angular separation than the simultaneously re-corded adjacent orders (k and k+1) of grating site 1. The previously discussed (Section 3.5) increase in estimated strain uncertainty (0.002 in/in versus 0.0045 in/in) due to this difference is borne out in examining the random deviations of the individual curves off the zero strain axis in the zero to fifty microseconds time interval before the arrival of the strain waves at these sites. The negative trend of the strains in this interval is not deemed significant since other cases exhibited a similar positive trend. Since this favored situation was maintained throughout the investigation, the results obtained at grating site 2 consistently showed the better correspondence in all tests; how-ever, the results shown in Figure 4.2.2 represent the "worst case" fit seen at grating site 1 for all the experiments.

The capability of the system to reproduce test conditions (impact velocity and axiality of impact) is also shown in the curves of Figure 4.2.1. The strain histories evidenced by the three experiments show excellent agreement in the loading and unloading positions of the curves and only a small deviation (0.5%) of Exp 6-15 at the apex from the re-sults of the other two experiments. Since the results of Figure 4.2.4 also show the maximum value of Exp 6-15 to exceed those of the other two experiments, it is believed that this deviation represents a slight change in impact conditions. The exact cause of the deviation is indeterminable since no monitoring of the axiality of impact was carried out. Although the pairs of duplicate experiments in the other cases evidenced the closer correspondence shown in Figure 4.2.1 by Exp 8-17 and Exp 3-27, the results of Exp 6-15 were accepted and included in the comparisons of the following sections.

In summary, the data obtained from grating site 2 showed the best agreement with correlations, during the recording of the strain pulse, which were indicated to be better than the estimated strain uncertainty of 0.002 in/in. The results obtained at grating site 1 were less quantitative and in some cases evidenced the full estimated uncertainty of 0.0045 in/in. In light of these observations, the results of grating site 2 were used for quantitative evaluations, whereas the results obtained at grating site 1 were used for less quantitative companion evaluations of observed trends.

4.3 An Indicated Equivalence

As noted in the review of the literature (section 1.3) previous investigations of the late-stage equivalence principle have been directed at evaluating its validity for various projectile shapes and projectile-target materials. In all of these investigations, target geometry was confined to that described analytically as a semi-infinite solid. More realistically, this target configuration is described as a flat plate having lateral dimensions which are much larger than the projectile dimensions and remove the influence of wave propagation from the target lateral surfaces upon the observed phenomenon. In the studies utilizing the extreme projectile configurations of a thin striker plate having infinite lateral dimensions, the influence of the projectile's lateral surfaces is also removed. This investigation proposed to test the validity of the principle for projectile and target having equal lateral dimensions which were approximately the same as the projectile lengths and could strongly affect the shock waves initiated by the impact; hence, it was felt that the previously determined values of α offered no guidance as to the existence of late-stage equivalence for this configuration.

This difficulty was obviated by employing the following search technique:

1)   A set of reference surface strain histories was collected from targets experiencing an arbitrarily chosen set of impact conditions (projectile length L_o, and impact velocity, V_o).

2)   A new velocity level (V_1) was selected and sets of corresponding surface strain histories collected from targets impacted by various lengths of projectiles (L_1's) at this nominal velocity level.

3)   Comparison plots of the results of 1) and 2) were used to evaluate trends and test for late-stage equivalence.

For all cases, strain-time information was obtained simultaneously at two axial positions on the target rods using reflective diffraction gratings separated by an axial distance of one-half inch. These grating sites, hereafter referred to as grating site 1 and 2, were positioned on the outer circumference of the rods at 5 3/8 inch and 5 7/8 inch respectively, from the impact site. In each case, duplicate experiments were run to verify the observed strain histories with a total of three experiments run for the reference case and two each for the other cases.

The experimental results of each individual case were plotted to obtain an average-value strain his ory curve for each unique set of impact conditions (projectile length, L_1, and impact velocity, V_1). then comparison plots of these average value curves were used to evaluate the correspondence of the test cases with the reference case. The results of this investigation are shown in Figures 4.3.1 through 4.3.4.

Shown in Figure 4.3.1 are comparison plots or the strain histories at grating site 2 for the reference case and the first two cases. It

Grating Site 2 (5 7/8 in from Impact Site)

O Reference (L_o =.571 in, v_o =15,476 ft/sec)

△ Case 1 (L_1 =.571 in, v_1 =10,980 ft/sec)

□ Case 2 (L_1 =.662 in, v_1 = 11,180 ft/sec)

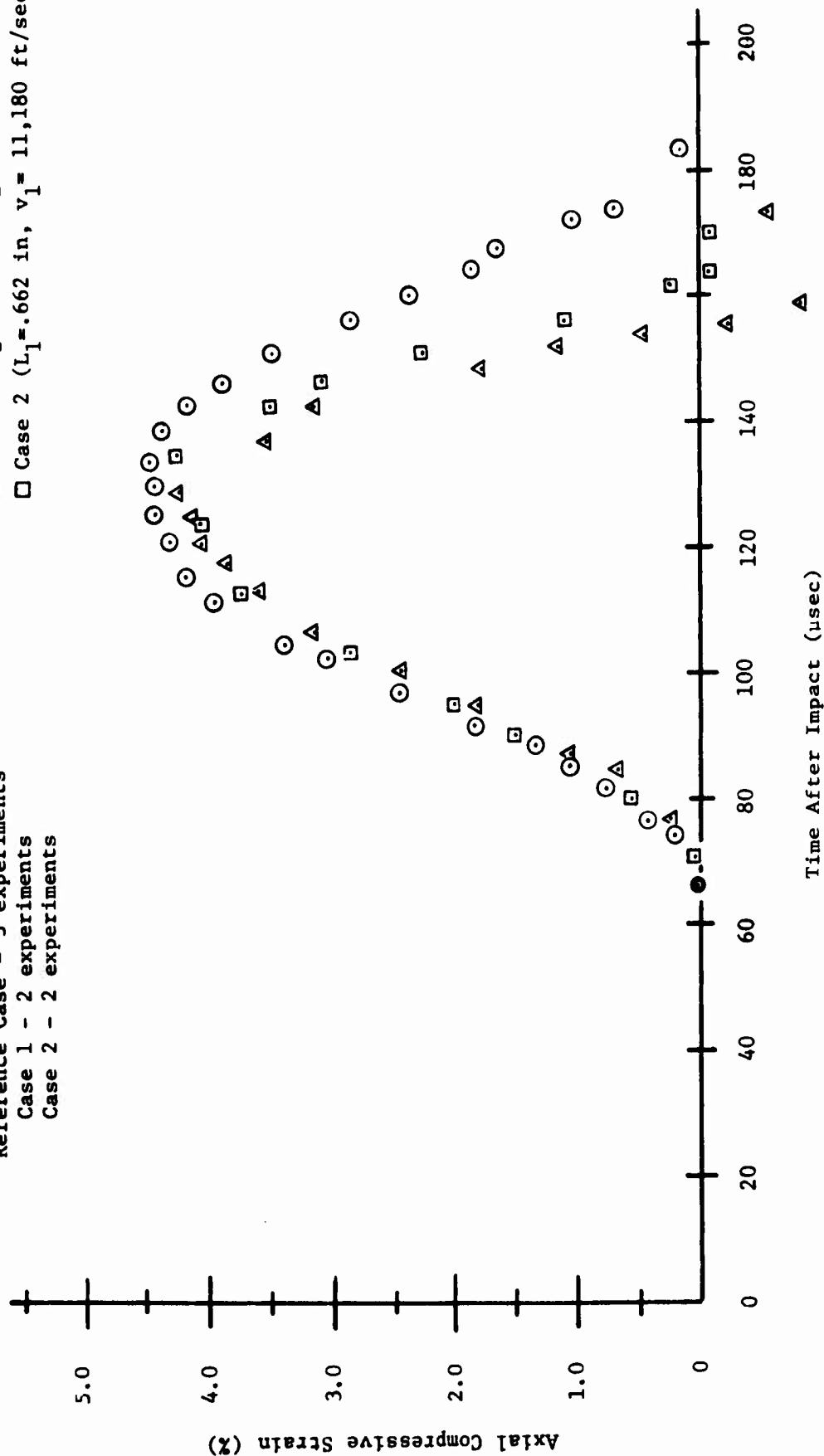Note: All curves are average value curves
Reference Case - 3 experiments
    Case 1 - 2 experiments
    Case 2 - 2 experiments

Time After Impact (µsec)

Axial Compressive Strain (%)

Figure 4.3.1 Comparison of Strain histories at grating site 2 for the reference case and Cases 1 and 2.
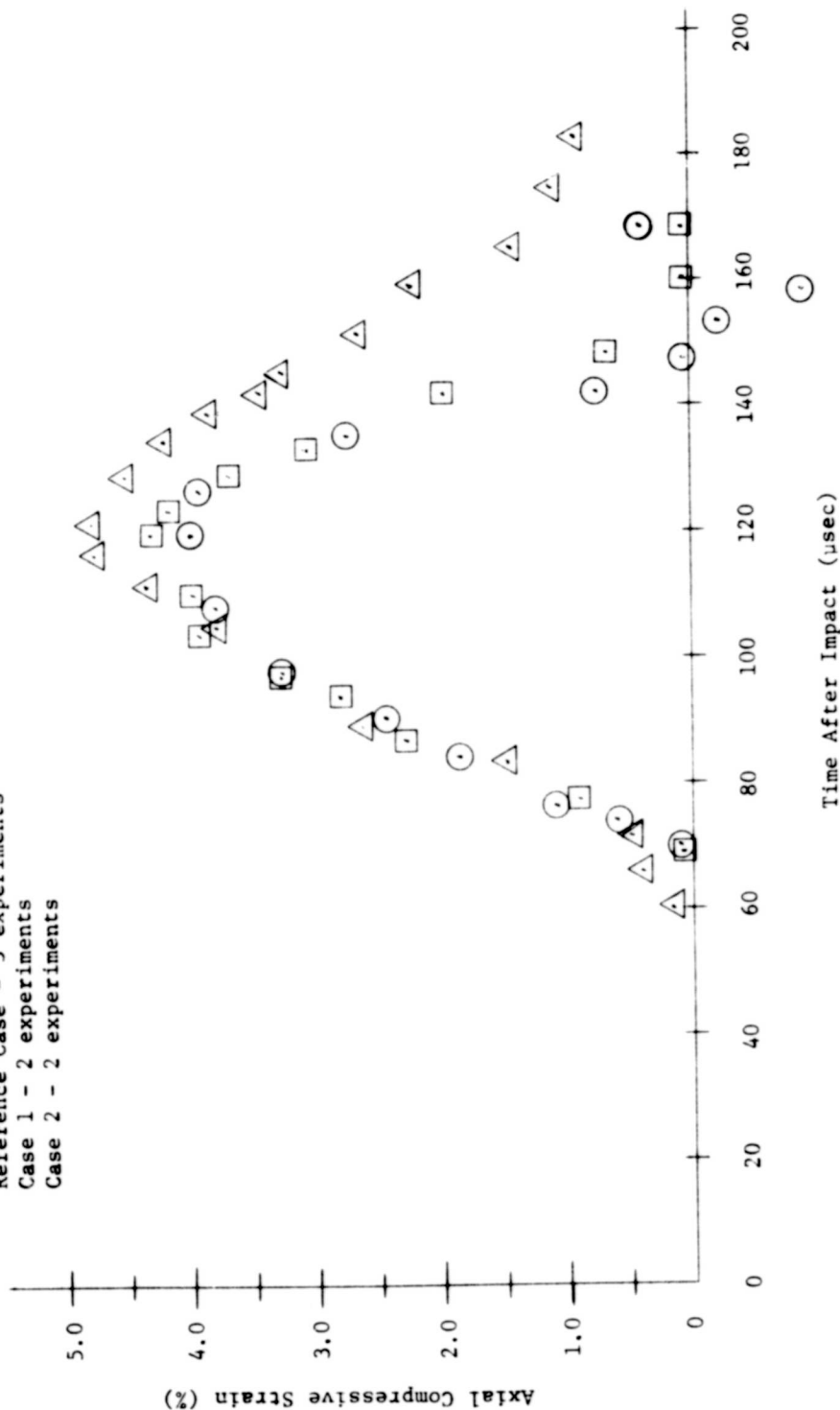
Figure 4.3.2 Comparison of strain histories at grating site 1 for the reference case and Cases 1 and 2.

Grating Site 2 (5 7/8 in from Impact Site)

○ Reference (L_o = .571 in, v_o = 15,476 ft/sec)

□ Case 3 (L_1 = .802 in, v_1 = 11,640 ft/sec)

Note: Both curves are average value
curves
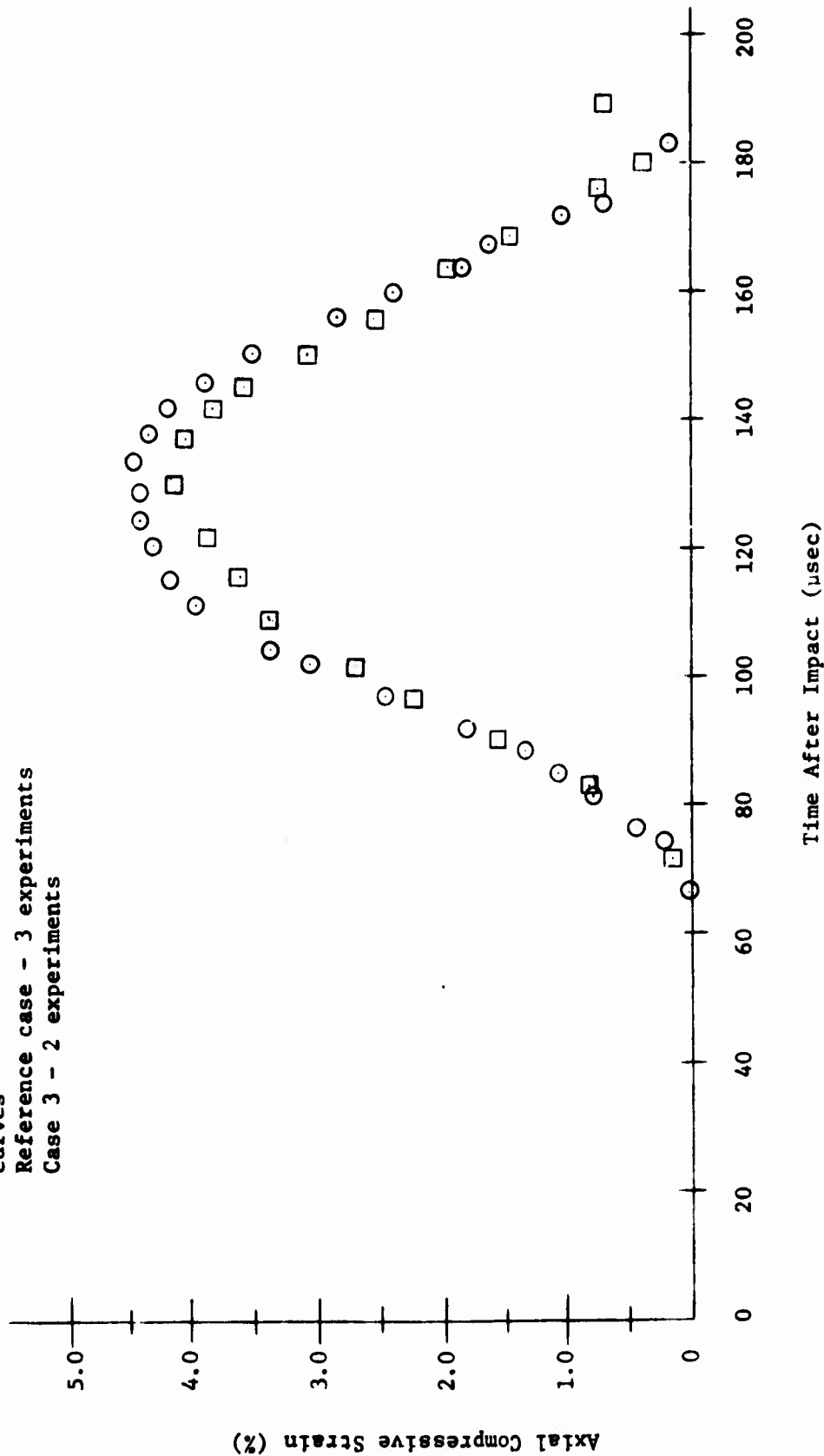Reference case - 3 experiments
Case 3 - 2 experiments

Axial Compressive Strain (%)

Time After Impact (μsec)

Figure 4.3.3 Comparison of strain histories at grating site 2 for the reference case and
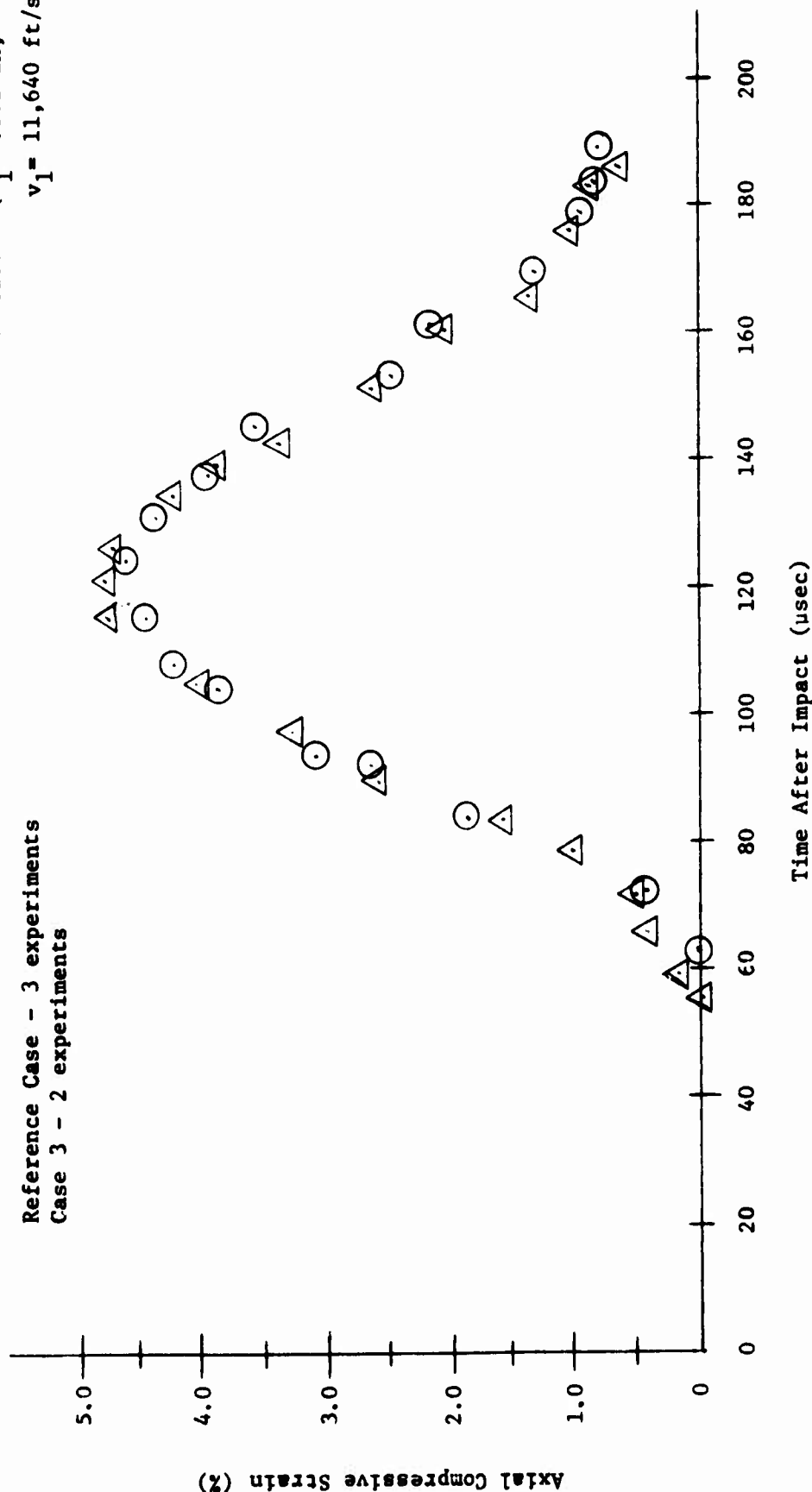Case 3.

Figure 4.3.4   Comparison of strain histories at Grating Site 1 for the reference case and Case 3.

should be noted that the maximum strain levels and wave arrival times, as indicated by the loading portion of the curves, is approximately the same for all three curves. Obviously, this dat₁ is out of the shock wave regime and the tests for late-stage equivalence used by Chou and Allison (14) (same peak pressure and wave arrival time) cannot be applied here. The main area of disparity is in the unloading portion of the curves and it is seen that as the projectile length is increased, the curves progress toward the reference curve. These trends are confirmed by the strain histories measured at grating site 1 and shown in Figure 4.3.2.

The results of these Figures (4.3.1 and 4.3.2) would indicate that a longer projectile at this velocity level would provide complete coincidence of the strain-time curves and establish equivalence with the reference case. Consider the comparison plots of case 3 with the reference case as shown in Figures 4.3.3 and 4.3.4. The strain histories measured at grating site 2 (Figure 4.3.3) show excellent agreement in the loading and unloading portions of the curves with a slight disparity in maximum values while the less quantitative results obtained at grating site 1 (Figure 4.3.4) show complete correspondence throughout the strain pulse.

The conclusion drawn from Figures 4.3.3 and 4.3.4 was that case 3 indicated but did not prove late-stage equivalence and a test case was conceived and performed to test the validity of the indicated equivalence.

4.4 Confirmation of the Indicated Equivalence

In order to verify the equivalence indicated by Figures 4.3.3 and 4.3.4, the impact conditions of the reference case and case 3 were used to predict a set of new impact conditions for a test case. This was accomplished in the following manner:

1) The impact conditions (L_1 and V_1) of the reference case and case 3 were substituted into the expression $L_o V_o^\alpha = L_1 V_1^\alpha$ to determine a value of α.

2) A new velocity level (approximately midway between the reference case and case 3 was selected and this value (V_2), along with the calculated value of α and the impact conditions of the reference case (L_o and V_o), were used to determine the required projectile length L_2.

Strain histories were then measured in two experiments from targets experiencing these new impact conditions (L_2 and V_2) for a comparison with the reference case values.

For this particular set of tests, data was recorded only at grating site 2 in order to capture the maximum number of diffracted rays from this grating site and provide accurate results for a comparison with the more quantitative results of the reference case at this axial location.

The results of this test case are shown in Figures 4.4.1 and 4.4.2 with comparisons shown for the average value curve of the reference case as well as for the individual curves of the reference case. The degree of coincidence of the curves is considered significant and it is considered that these results confirm the existence of late-stage equivalence for this new target geometry.

Inserting the impact conditions of the reference case and case 4 into the scaling law ($L_o V_o^\alpha = L_1 V_1^\alpha$), the value of α is found to be 1.32. It is noted that this value is in the range of values previously determined for the one-dimension plane wave case of the thin striker plates of infinite lateral dimensions impacting a semi-infinite solid and, in fact, practically coincides with value determined for 1100F aluminum in the plane wave case. Based on the previous discussions in Section 1.3
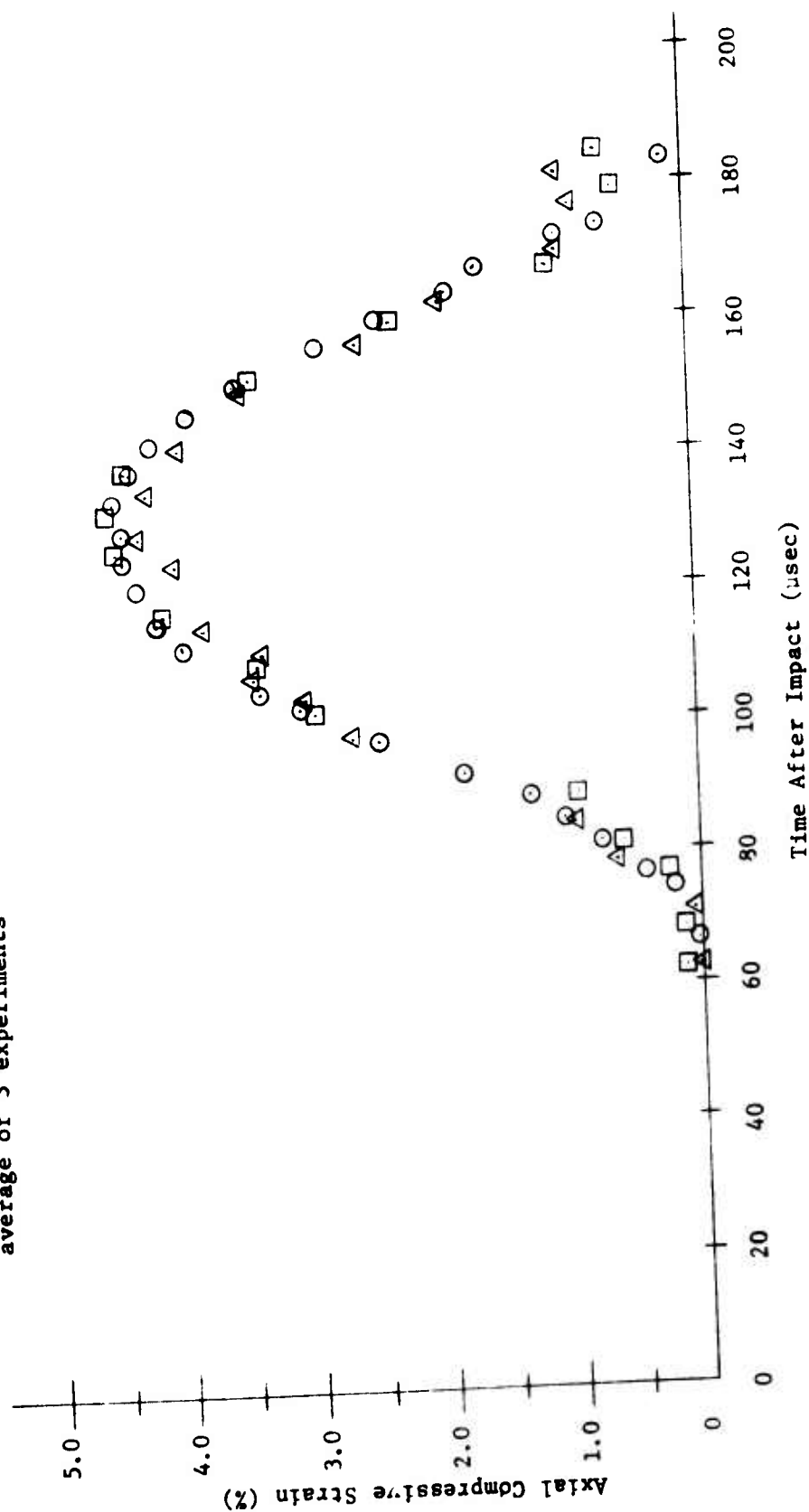
Figure 4.4.1 Comparison of strain histories at grating site 2 for the reference case average value curve and the two experiments of Case 4.
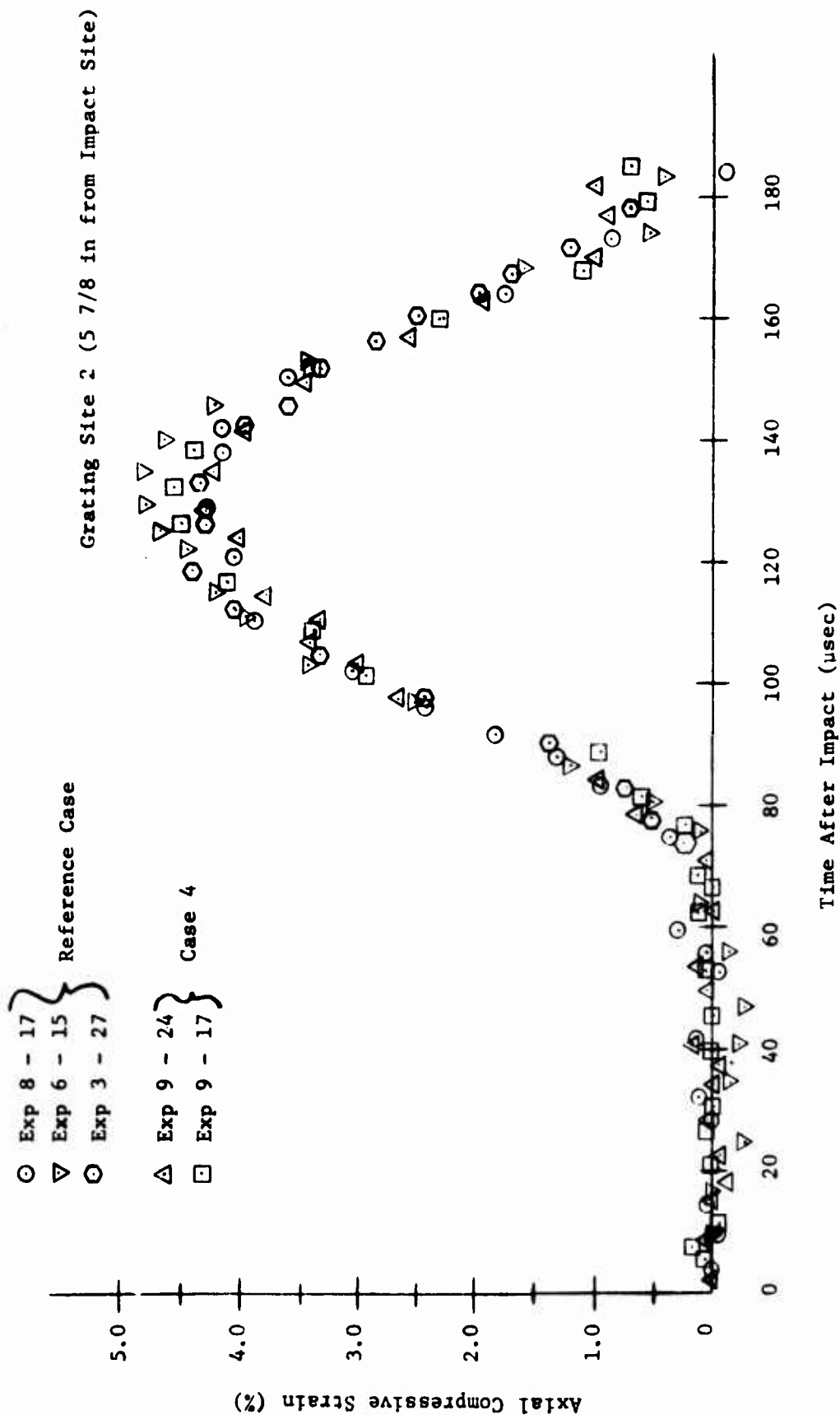
Figure 4.4.2 Comparison of individual strain histories at grating site 2 measured for the reference case and Test Case 4.

of the shift in bounding values of the exponents of momentum and energy from 1/3 and 2/3 respectively, (for the axisymmetric case) to 1 and 2, respectively, (for the plane wave case), this result is to be expected. Contained in the derivation of Equations 1.3.9 through 1.3.10 was the assumption that the projectiles have fixed lateral dimensions, which also applies to this investigation since only the projectile lengths were varied. Hence, it is not too surprising that the value of the exponent conforms more to the plane wave configuration than to the axisymmetric case.

4.5 Definition of the Target Geometry

Due to the presence of the gas and debris baffles around the target rod (shown in Figure 3.2.5), it was decided to try to evaluate the influence of these baffles upon the measured strain histories. In an attempt to determine these effects, a series of experiments was proposed which would duplicate the impact conditions (L_i and V_i) of each case but the target rod would be initially positioned a half-inch forward; hence, the axial positions of the baffles with respect to the impact face would be changed and it was expected that any influences of these lateral constraints would be evidenced in the resulting strain histories.

Results were obtained only for cases 1, 2, and 3. The requisite increases in launch tube gas pressures needed to attain the higher level impact velocities of case 4 and the reference case resulted in gas leaks of the baffle system for this positioning of the target rod. Minor modifications of the baffle system did not stop the gas leaks and since it was felt that major modifications would destroy the validity of the results, no further attempt was made to obtain results for these cases.

Grating Site 2

△ Average value curve of Case 1 – standard

⊙ Test Case Results

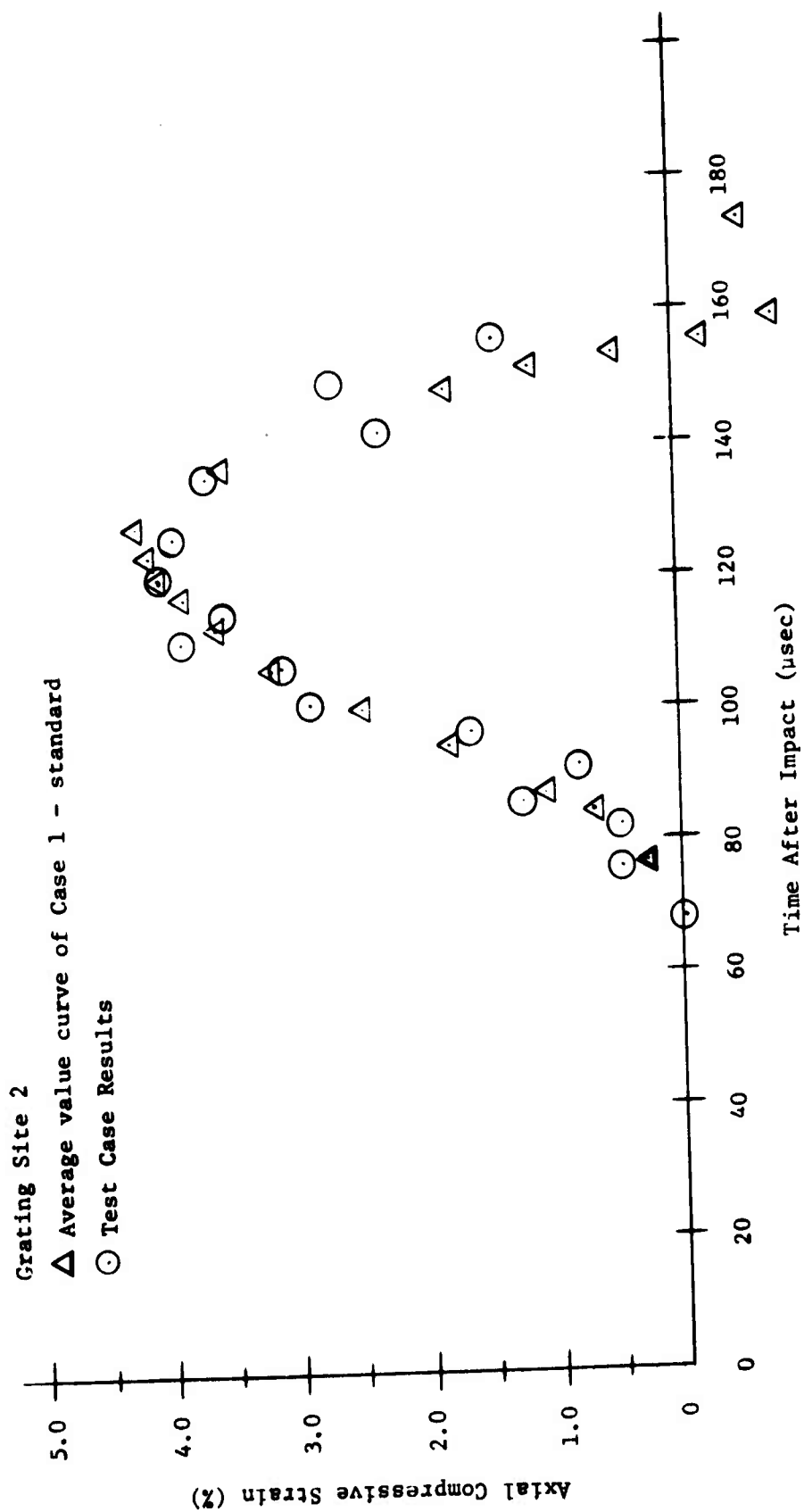Axial Compressive Strain (%)

Time After Impact (μsec)

Figure 4.5.1 Comparison of Case 1 strain histories at grating site 2
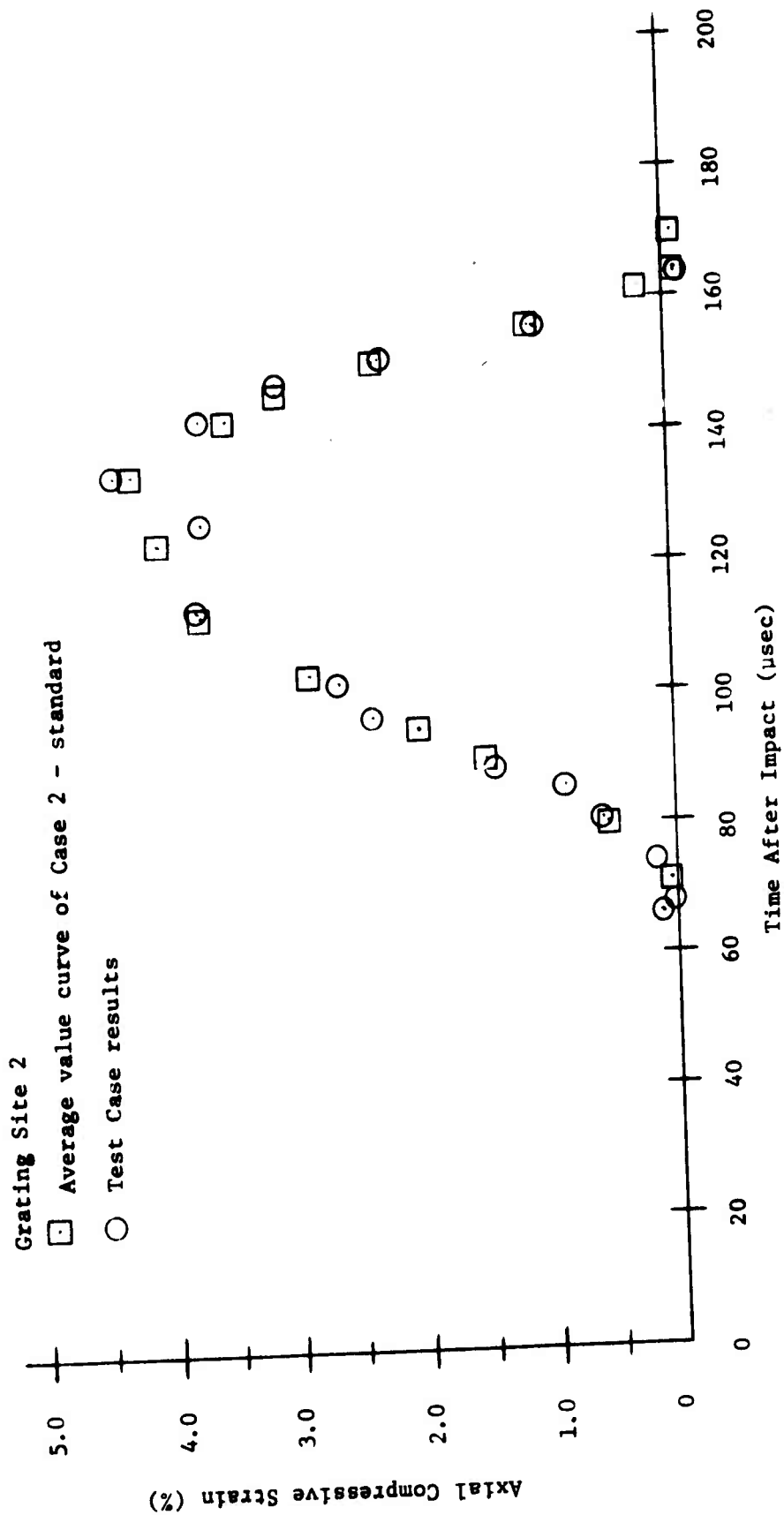for the standard and test positions of the target rods.

Figure 4.5.2 Comparison of Case 2 strain histories at grating site 2 for the standard and test positions of the target rods.
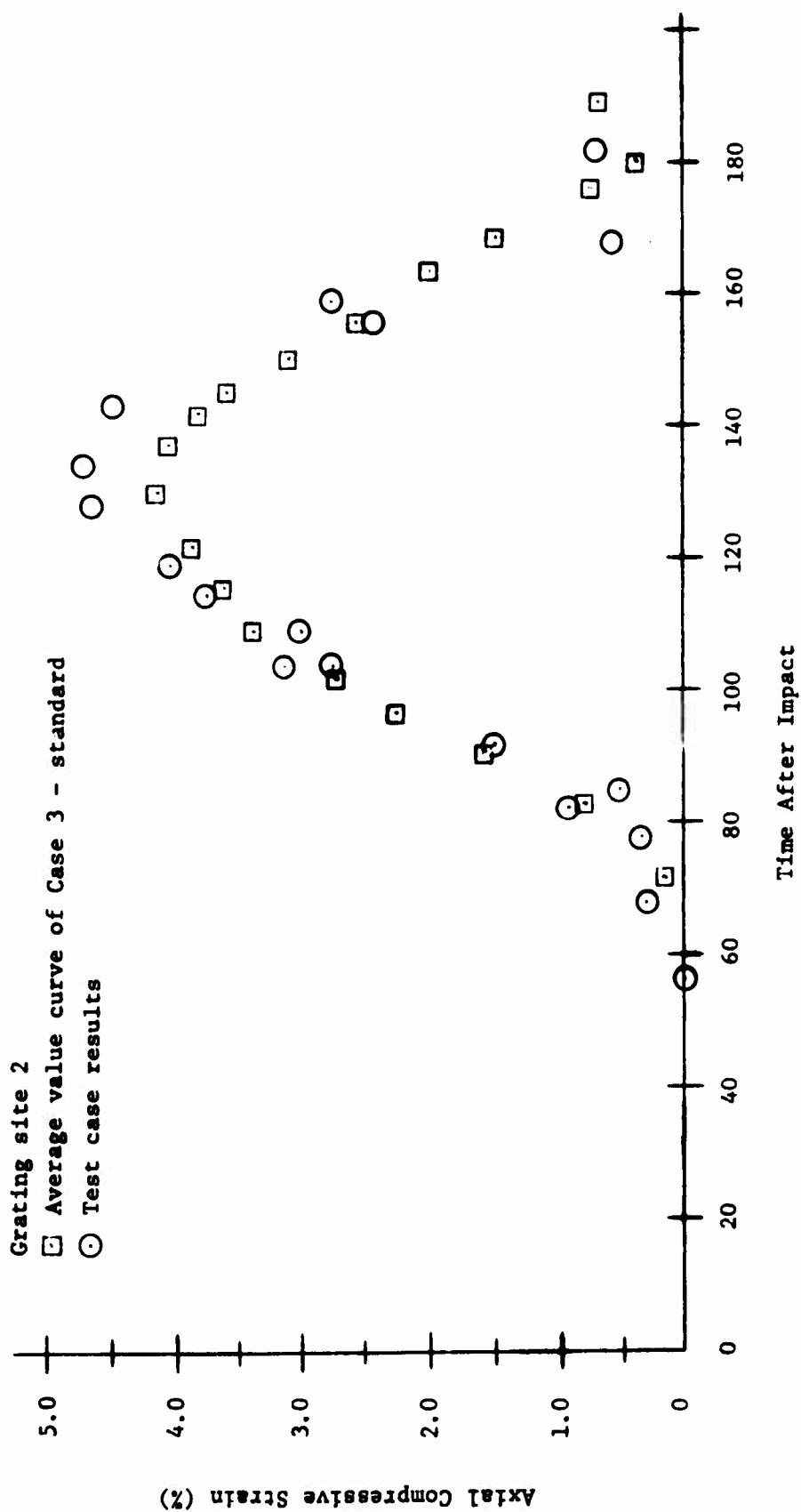
Figure 4.5.3 Comparison of Case 3 strain histories at grating site 2 for the standard and test positions of the target rods.

The results for cases 1 through 3 are shown in Figures 4.5.1 through 4.5.3. Since the forward positioning of the rods moved the grating site to the former optical position of grating site 1, only adjacent orders were recorded and the reduced results have an estimated uncertainty of 0.0045 in/in. Within the resolution of these results, the strain histories for these cases appeared to be the same. This was expected since an amount of target rod was positioned far enough forward of the front surface of the primary gas cup (4 radii) so as to exceed the previously measured wave arrival distances of Di Battista (17); however, in the absence of information about case 4 and the reference case, it was concluded that the target geometry could not be positively described as that of a rod.

It is felt, however, that this does not limit the significance of the results, since if the influences of the baffles must be included in the target geometry, the new target described by the complete system of Figure 3.2.5 represents an even more radical departure from a semi-infinite solid target than does a target having the more uniform lateral dimensions of a rod.

4.6 Conclusions

Using reflective diffraction gratings as strain transducers, a system was developed to measure axial surface strains in polycarbonate target rods experiencing axial hypo and hypervelocity impact by equal diameter short polycarbonate projectiles. Due to the requisite placing of baffles around the target rods between the impact site and the grating sites, information was gathered only in the strength affected (elastic) zones, yet strains of 5% were easily recorded simultaneously from two axial positions on the rod.

This system was used to investigate the validity of the late-stage equivalence principle for this new target configuration. Analysis of the experimental results leads to the following conclusions:

1) Comparison of the measured transient deformations indicates that late-stage equivalence does apply to this configuration.

2) From the impact conditions of those targets exhibiting late-stage equivalence, the value of the exponent α in the scaling law, $L_o V_o^{\alpha} = L_1 V_1^{\alpha}$, is calculated to be 1.32.

3) The influence of the requisite impact tube baffles upon the observed results is not known, but it is not felt that this influences the significance of the results since the inclusion of these lateral restraints in the target geometry would result in a target even more radically different than the previously investigated semi-infinite solid targets.

5 List of References

1. Frasier, J. T. and Karpov, B. G. 1965. The Transient Responses of Wax Targets Subjected to Hypervelocity Impacts. Exp. Mech. 5(9): 305-312.

2. Walsh, J. M. and Tillotson, J. H. 1966. Hydrodynamics of Hypervelocity Impact. General Atomic Division of General Dynamics Report GS-3827.

3. Eichelberger, R. J. 1965. Behavior of Materials Under Dynamic Loading, pp 155-187, (Huffington, ed.). The American Society of Mechanical Engineers, New York.

4. Dienes, J. K. and Walsh, J. M. 1970. High Velocity Impact Phenomena, pp 45-104. (Kinslow, ed.). Academic Press, New York.

5. Rae, W. J. 1970. High Velocity Impact Phenomena, pp 214-286, (Kinslow, ed.). Academic Press, New York.

6. Yuan, S. W. and Bloom, A. M. 1964. An Analytical Approach to Hypervelocity Impact. AIAA J.2: 1667-9.

7. Yuan, S. W. and Scully, C. N. 1963. A New Approach to Hypervelocity Impact Theory. Adv. Astronaut. Sci. 13: 599-615.

8. Bjork, R. L. 1958. Effects of Meteoroid Impact on Steel and Aluminum in Space. Rand Corp. Paper 1662.

9. Rae, W. J. and Kirchner, H. P. 1963. A Blast-Wave Theory of Crater Formation in Semi-infinite Targets. Proc. of Sixth Symp. on Hypervelocity Impact, vol 2, pt 1, pp 163-228.

10. Rae, W. J. and Kirchner, H. P. 1963. Final Report on a Study of Meteoroid Impact Phenomena. Cornell Aeronautical Lab. Rept. Rm-1655-m-4. Buffalo, New York.

11. Frasier, J. T. 1968. The Transient Response of Targets Subjected to Hypervelocity Impacts. Mech. of Solid State, pp 36-48 (Parott and Schwaighofer, ed.) University of Toronto Press, Great Britain.

12. Dienes, J. K. 1964. Late-stage Equivalence and Similarity Theory for One-Dimensional Impacts, General Atomic Division of General Dynamics Report GA-5755 (Nov).

13. Chou, P. C. and Burns, B. P. 1967. Late-Stage Equivalence in One-Dimensional Impacts. JAP 38(2): 553-560.

14. Chou, P. C. and Allison, F. E. 1966. Strong Plane Shock Produced by Hypervelocity Impact and Late-Stage Equivalence. JAP 37(2): 853-860

15. Duvall, G. E. and Fowles, G. R. 1963. High Pressure Physics and Chemistry, pp 209-223, (Bradley, ed.). Academic Press, New York.

16. Al'Tshuler, L. V., Kormer, S. B., Brazhnik, M. I., Vladimirov, L.A., Speranskaya, M. P. and Funtikov, A. I. 1960. The Isentropic Compressibility of Aluminum, Copper, Lead and Iron at High Pressures. Soviet Physic JETP 11(4): 766-775.

17. Di Battista, J. D. 1968. Shock Wave Pressure Decay in Polycarbonate Targets Impacted by Cylindrical Polycarbonate Projectiles. NASA Technical Note, NASA TN D-4864.

18. Teinecke, W. G. and McKay, W. L. 1969. Hypervelocity Impact of Small Right Circular Cylinders. AIAA J. 1(10): 1921-1924.

19. Bell, J. F. 1968. The Physics of Large Deformations of Crystalline Solids. Springer, Verlag, Berlin, Heidelberg, New York.

20. Bell, J. F. 1969. The Dynamic Plasticity of Non-Symmetrical Free Flight Collision Impact. Int. Journal of Mechanical Sciences 11(8): 633-657.

21. Liddell, W. L., Steele, R. S., Bingham, W. L. and Douglas, R A. 1970. Experimentally-Determined Plastic Wave Velocities in Polycarbonate. 1970. Contract N00014-68-A-0187, Tech. Report 70-10, U. S. Government Printing Office, Washington, D. C.

22. Liddell, W. L., Steele, R. S., Bingham, W. L. and Douglas, R. A. 1970. Experimentally-Determined Plastic Wave Velocities in Fully-Annealed 1100F Aluminum. Contract N00014-68-A-0187, Tech. Report 70-11. U. S. Government Printing Office, Washington, D. C.

23. Liddell, W. L., Steele, R. S., Bingham, W. L. and Douglas, R. A. 1971. Experimental Investigation of Large-Amplitude Elastic Wave Propagation and the Elastic-Plastic Transition in Polycarbonate (Lexan). Contract N00014-68-A-0187, Tech. Report 71-6. U. S. Government Printing Office, Washington, D.C.

24. Valather, M. and Baker, W. B. 1971. Wave Propagation from Very High Impact Velocities. J. Appl. Mech. 38(2): 555-557.

25. Jenkins, F. A. and White, H. E. 1957. Fundamentals of Optics. McGraw-Hill, New YOrk.

26. Liddell, W. L. 1973. An Experimental Investigation of Large-Amplitude Wave Propagation and Dynamic Elastic Properties in Longitudinally-Impacted Polycarbonate Rods. Phd Diss., N. C. State Univ., Raleigh, N. C.

27. Blake, H. W., Stadelmaier, H. H. and Douglas, R. A. 1969.
    Diffraction of Light by a Grating Subjected to Homogeneous
    Strains and Rigid Body Rotations. Contract N00014-68-A-0187,
    Tech. Report 69-8. U. S. Government Printing Office,
    Washington, D. C.

28. Curtis, John 1964. An Analysis of the Interior Ballistics of
    the Constant Base Pressure Gun. G. E. Defense Research Labs,
    Santa Barbara, Calif. TR64-27.

29. Jeelani, S., Kelly, J. J., Whitfield, J. K. and Douglas, R. A.
    1973. Two-Stage Light-Gas Gun Installation for Hypervelocity
    Impact Studies. Contract N00014-68-A-0187, Tech. Report 73-3.
    U. S. Government Printing Office, Washington, D. C.

30. Cadillac Plastic and Chemical Co. Bonding of Polycarbonate.
    15111 2nd Ave, Detroit, Mich.

31. Holman, J. P. 1966. Experimental Methods for Engineers. McGraw-
    Hill Book Company, Inc. New York.